HHS Public Access

Author manuscript

*Nat Microbiol*. Author manuscript; available in PMC 2024 March 25.

Published in final edited form as:

*Nat Microbiol*. 2023 October ; 8(10): 1880–1895. doi:10.1038/s41564-023-01459-y.

# The Parkinson's disease kinase LRRK2 coordinates a cell intrinsic defense pathway against the intracellular pathogen *Salmonella*

**Huan Lian**[1,4,5], **Donghyun Park**[1,2,4,6], **Meixin Chen**[1,7], **Florian Schueder**[1,3], **Maria Lara-Tejero**[1], **Jun Liu**[1,2], **Jorge E. Galán**[1,*]

[1]Department of Microbial Pathogenesis, Yale University School of Medicine, New Haven, CT06536

[2]Microbial Science Institute, Yale University School of Medicine, New Haven, CT06536

[3]Department of Cell Biology, Yale University School of Medicine, New Haven, CT06536

[4:]contributed equally to this work

[5:]Present address: Department of Laboratory Medicine, Zhongnan Hospital of Wuhan University, Medical Research Institute, Frontier Science Center for Immunology and Metabolism, Wuhan University, Wuhan 430071, China.

[6:]Present address: Department of Integrative Structural and Computational Biology, Scripps Research, MB 113, 10596 N Torrey Pines Rd, La Jolla, CA 92037

[7:]Present address: Institute of Infectious Diseases, Shenzhen Bay Laboratory, Shenzhen, Guangdong, China

## Abstract

Cell intrinsic defenses constitute the first line of defense against intracellular pathogens. The guanosine triphosphatase (GTPase) RAB32 orchestrates one such defense response against the bacterial pathogen *Salmonella,* through delivery of antimicrobial itaconate. Here we show that the Parkinson's disease (PD) associated leucine rich repeat kinase 2 (LRRK2) orchestrates this defense response by scaffolding a complex between RAB32 and aconitate decarboxylase 1 (IRG1), which synthesizes itaconate from mitochondrial precursors. Itaconate delivery to Salmonella-containing vacuoles (SCVs) was impaired and *Salmonella* replication increased in LRRK2-deficient cells. Loss of LRRK2 also restored virulence of a *Salmonella* mutant defective in neutralizing this RAB32-dependent host defense pathway in mice. Cryo-electron tomography revealed tether formation between SCVs and host mitochondria upon *Salmonella* infection, which was significantly impaired in LRRK2-deficient cells. This positions LRRK2 centrally within a

[*]for correspondence: jorge.galan@yale.edu.

Author Contributions

H. L. performed the functional and biochemical experiments; D. P. conducted all the cryo-ET experiments with the assistance of H. L., M. C. and under the direction of J. L.; F. S. performed the DNA-PAINT imaging experiments; M.L.-T. performed the LC—MS/MS experiments and coordinated the animal experiments; J.E.G. conceived and directed the project and wrote the manuscript with comments from all the authors.

**Competing Interests Statement** All authors declare no competing interests

host defense mechanism, which may have favored selection of a common familial PD mutant alleles in the human population.

**Keywords**

Parkinson's disease; innate immunity; bacterial pathogenesis; *Salmonella* pathogenesis; *Salmonella* Typhi; typhoid fever; host defense; itaconate; mitochondria; SLC25A1; citrate carrier; CIC; aconitate decarboxylase 1; ACOD1; IRG1; RAB32; cell autonomous immunity; Rab GTPases; cryo electron-tomography; inter-organelle communication

Many cells, particularly those of hematopoietic origin, have the intrinsic capacity to control bacterial infections in a manner independent from but synergistic with the immune system[1]. RAB32 is involved in one such mechanism, which is central for the control of intracellular pathogens including the human-adapted pathogen *Salmonella enterica* serovar Typhi (*S.* Typhi), the causative agent of typhoid fever[2–6]. RAB32 exerts its function by facilitating the delivery of the antimicrobial compound itaconate to the SCV[6,7]. Itaconate is synthesized by aconitate decarboxylase 1 (also known as IRG1) from cis-aconitate, a tricarboxylic acid cycle intermediate produced in the mitochondria[8]. This compound exerts its antimicrobial function by inhibiting methylmalonyl–coenzyme A (CoA) mutase[9], isocitrate lyase[10,11], and succinate dehydrogenase[12], which are essential for the metabolism of several intracellular pathogens including *Salmonella* and *Mycobacterium* spp.[13–20]. During evolution, pathogens have acquired mechanisms to counter host defenses[21,22]. Thus, the broad host range *Salmonella enterica* serovar Typhimurium (*S.* Typhimurium) can effectively neutralize this RAB32-dependent restriction mechanism by deploying two effectors of its type III protein secretion systems (T3SSs), SopD2 and GtgE, which directly target RAB32 with specific GAP and protease activities[2,23,24]. In addition, *S.* Typhimurium encodes a set of enzymes that can specifically degrade itaconate[25,26], which like SopD2 and GtgE, are absent from the human adapted *S.* Typhi[27].

How RAB32 coordinates the delivery of itaconate to the SCV is unclear although its ability to form a complex with IRG1 is predicted to be central to this mechanism[6]. RAB32 also interacts with the Parkinson's disease (PD) associated kinase LRRK2 [28,29], which like RAB32[2,30,31], localizes to the mitochondria[32], is recruited to the SCV[33], and has been shown to be important for the control of intracellular pathogens like *Salmonella* and *Mycobacterium* spp.[34–37]. On the other hand, like LRRK2, mutations in RAB32 have been linked to familial PD[38], further suggesting a connection between this mechanism of host defense and PD. In fact, other proteins associated with PD, like Parkin and Pink1, have also been linked to both pathogen resistance and mitochondria physiology[39–41]. Here, we have examined the potential link between LRRK2 and the Rab32-dependent host defense pathway. We found that LRRK2 is required for itaconate delivery to the SCV. We also found that LRRK2-deficient cells can sustain greater intracellular *Salmonella* replication, and that LRRK2-defficient mice can rescue the virulence phenotype of a *S.* Typhimurium Δ*gtgE* Δ*sopD2* mutant strain specifically defective in its ability to block itaconate delivery to the SCV. Furthermore, we found that the SCV and the mitochondria establish a close association mediated by multiple tethers, which are absent in LRRK2-defficient cells. Our studies indicate that LRRK2 plays a central role in intracellular pathogen host defense, thus

potentially linking PD and differential susceptibility to microbial pathogens as a potential driver for the selection of one of the most common familial PD mutant alleles in the human population.

## Results

### LRRK2 is required for itaconate delivery to SCVs

We first examined the delivery of itaconate to the SCV in CRISPR/Cas9-generated LRRK2-deficient Raw264.7 macrophages and DC2.4 dendritic cells (Fig. 1a). We chose these cells because our previous studies have shown that they robustly express the RAB32-dependent defense pathway[6]. To monitor itaconate delivery to the SCV we used an itaconate biosensor we have previously developed[6]. This biosensor is based on luciferase or fluorescent protein (GFP or mCherry) reporters whose expression in *Salmonella* is strictly dependent on a transcription factor that, by directly sensing the presence of itaconate, controls the expression of an itaconate degradation pathway. We found that, compared to parental cells, expression of the luciferase or GFP itaconate reporters was significantly reduced in LRRK2-deficient cells infected with *S.* Typhi (Fig. 1b, 1d, and Extended Data Fig. 1a and 1b). We also found that itaconate delivery was impaired in LRRK2-deficient cells infected with a *S.* Typhimurium Δ*gtgE* Δ*sopD2* mutant strain (Fig. 1c), which is specifically defective in its ability to neutralize the RAB32 defense pathway[2,23]. Importantly, the absence of LRRK2 did not affect the levels of itaconate after lipopolysaccharide (LPS) stimulation, indicating that it is not required for itaconate synthesis (Fig. 1e). Taken together, these results indicate that LRRK2 is required for efficient itaconate delivery to the SCV.

We have previously shown that growth of the human-adapted *S.* Typhi in mouse macrophages is restricted, and that such restriction is removed in mouse Raw264.7 and DC2.4 cells lacking either RAB32, its exchange factor BLOC3[2], or IRG1[6]. Similarly, we found that, despite the presence of equal number of bacteria to those in parental cells immediately after infection (Extended Data Fig. 1c–g), *S.* Typhi loads in LRRK2-defective Raw264.7 and DC2.4 cells, or in bone marrow derived mouse macrophages (BMDMs) obtained from *Lrrk2*$^{-/-}$ mice were much higher 20 hs after infection (Fig. 1f–h). In fact, these bacterial loads were almost as high as those of wild-type *S.* Typhimurium (Fig. 1i), which can efficiently block the RAB32 defense pathway and, consequently, replicate within these cells. These results indicate that LRRK2 restricts *S.* Typhi intracellular replication in non-permissive host cells. We have previously shown that the *S.* Typhimurium Δ*gtgE* Δ*sopD2* mutant strain, which is unable to neutralize the RAB32 defense pathway, has reduced ability to grow within Raw264.7 and DC2.4 cells, as well as primary BMDMs[2,23], a phenotype that was reversed in the same cells lacking either RAB32 or IRG1[6]. Similarly, we found that the growth defect of this mutant strain was reversed in Raw264.7 cells lacking LRRK2 or in *Lrrk2*$^{-/-}$ BMDMs (Fig. 1j and 1k). We also tested the virulence phenotype of wild-type and Δ*gtgE* Δ*sopD2 S.* Typhimurium strains in *Lrrk2*$^{-/-}$ mice. We found that, as previously shown[34,35], *Lrrk2*$^{-/-}$ mice were more susceptible to wild-type *S.* Typhimurium infection (Fig. 1l). Importantly, however, the virulence defect of the *S.* Typhimurium Δ*gtgE* Δ*sopD2* mutant strain was substantially reversed in *Lrrk2*$^{-/-}$ mice (Fig. 1m). Taken together,

these results indicate that LRRK2 is an intrinsic component of the RAB32-host defense pathway against *Salmonella* infection.

## LRRK2 kinase activity is required for itaconate delivery to the SCV

To gain insight into the mechanisms by which LRRK2 contributes to the RAB32-dependent host defense pathway, we examined the potential contribution of its kinase activity. We found that *S*. Typhimurium infection of Raw264.7 macrophages resulted in the rapid phosphorylation of LRRK2 at its residue S935 (Fig. 2a), which is a measure of its activation[42]. Equivalent results were found in DC2.4 cells (Extended Data Fig. 2). We also found that the ability of *S*. Typhimurium to activate LRRK2 was independent of its T3SS encoded within its pathogenicity island 1 (SPI-1)[43], as a Δ*invA* mutant strain, which is defective in this system[44], was equally able to activate this kinase (Fig. 2a). Most likely, LRRK2 activation is stimulated by *Salmonella* lipopolysaccharide (LPS), since addition of purified LPS resulted in a similar level of activation (Fig. 2a and Extended Data Fig. 2), and cultured cells that do not respond to LPS infected with wild-type *S.* Typhimurium did not show kinase activation (Fig. 2b). To specifically investigate the potential contribution of its kinase activity to the RAB32-defense pathway, we examined the effect of the highly specific LRRK2 kinase inhibitor GSK2578215A[45] on the delivery of itaconate to the SCV. We found that addition of the LRRK2 kinase inhibitor significantly impaired itaconate delivery to the *S.* Typhi containing vacuole (Fig. 2c). Similar results were observed in Raw264.7 cells infected with the *S*. Typhimurium Δ*gtgE* Δ*sopD2* mutant (Fig. 2d). Consistent with the impaired itaconate delivery, Raw264.7 and DC2.4 cells treated with the LRRK2 kinase inhibitor sustained greater bacterial replication when infected with *S*. Typhi or the *S*. Typhimurium Δ*gtgE* Δ*sopD2* mutant (Fig. 2e and 2f). These results indicate that the kinase activity of LRRK2 contributes to the RAB32-dependent pathogen restriction pathway.

## LRRK2 scaffolds the formation of Rab32-Irg1 complexes

In addition to its kinase domain, LRRK2 contains several protein-protein interaction domains including the Ras of complex (ROC) GTPase domain, a WD40 domain, and a series of armadillo, ankyrin, and leucine rich repeats[46]. This structural organization makes this kinase an ideal scaffolding protein to potentially organize signaling or other functional protein complexes[47]. LRRK2 has been shown to directly interact with RAB32 *in vitro*[29], and both, LRRK2[33] and RAB32[2], have been shown to be robustly recruited to the SCV. We therefore investigated whether these two proteins could form a complex upon *Salmonella* infection. We infected cells expressing FLAG-tagged RAB32 and GFP-tagged LRRK2 and examined their interaction by co-immunoprecipitation. We found that, consistent with their *in-vitro* interaction[29], LRRK2 formed a complex with RAB32 *in vivo* (Fig. 3a and 3b and Extended Data Fig. 3a). Importantly, formation of the complex was significantly enhanced by bacterial infection (Fig. 3a and 3b and Extended Data Fig. 3a). We then examined the ability of LRRK2 to form a complex with IRG1 by infecting cells expressing FLAG-tagged IRG1 and GFP-tagged LRRK2. We found that LRRK2 formed a complex with IRG1 and, as we observed with RAB32, the formation of the complex was significantly enhanced by *Salmonella* infection (Fig. 3c and 3d and Extended Data Fig. 3b). Formation of these complexes was also detected with endogenous proteins (Fig. 3e and Extended Data Fig. 3c, 3f, and 3g). The ability of LRRK2 to form a complex with RAB32 or Irg1 did not require its

kinase activity since addition of the LRRK2 kinase inhibitor (Extended data Fig. 3c and 3d) or expression of kinase-defective or constitutively active forms of LRRK2 (Extended data Fig. 3e) did not affect the formation of these complexes.

Since we have previously shown that RAB32 forms a complex with IRG1 upon *Salmonella* infection[6], we examined whether the formation of this complex was dependent on LRRK2. We infected parental Raw264.7 and a CRISPR/Cas9 generated LRRK2-deficient mutant derivative stably expressing FLAG-tagged RAB32 with the *S.* Typhimurium Δ*gtgE* Δ*sopD2* mutant strain and examined the interaction of RAB32 with endogenous IRG1 by co-immunoprecipitation. We found that the absence of LRRK2 resulted in a pronounced reduction in the levels of co-immunoprecipitation of RAB32 and IRG1, consistent with the notion that the formation of this complex is scaffolded by LRRK2 (Fig. 3e and 3f and Extended Data Fig. 3f and 3g).

To interact with one another, these proteins should be in the same subcellular compartment. As previously reported[6,30,32,48] we found that IRG1, LRRK2, and RAB32 localized to the mitochondrial fraction (Extended Data Fig. 4a and 4b), although the three proteins (including IRG1[49]) lack mitochondrial localization signals. We found that limited protease treatment of the mitochondrial fraction effectively eliminated IRG1, RAB32 and LRRK2, although it did not affect the levels of the matrix protein cytochrome C oxidase subunit 4 (Cox IV), which was readily degraded in the presence of detergent (Extended Data Fig. 4a and 4b). In addition, super-resolution microscopy with DNA **p**oints **a**ccumulation for **i**maging in **n**anoscale **t**opography (DNA-PAINT) showed that IRG1 did not co-localize with the mitochondrial matrix protein Cox IV (Extended Data Fig. 4c), suggesting that it is located either on the outer-surface or in the mitochondrial inter-membrane space, which our studies could not distinguish. More importantly, however, DNA-PAINT showed the co-localization of the three proteins at the SCV/mitochondria interface (Extended Data Fig. 4d and 4e).

The observation that IRG1 is located outside of the mitochondrial matrix suggests that, to synthesize itaconate, it must have access to its precursor, cis-aconitate, which would have to be transported out of the mitochondrial matrix, its place of synthesis. In this context it is intriguing that LRRK2 has been reported to interact with the mitochondrial tricarboxylate inner-membrane transporter SLC25A1 (also known as mitochondrial citrate carrier or CIC)[50–52], a member of the mitochondrial carrier subfamily of solute carrier proteins[53], which is a good candidate to transport cis-aconitate out of the mitochondrial matrix. Consistent with this hypothesis, addition of the SLC25A1 inhibitor CTPI-2[54] significantly impaired the delivery of itaconate to the SCV (Extended Data Fig. 5a and 5b), although it did not affect the expression of IRG1 (Extended Data Fig. 5c), nor did it impair the overall levels of itaconate synthesis (Extended Data Fig. 5d). The ability of LRRK2 to interact with IRG1 and SLC25A1 may facilitate the localized synthesis of itaconate prior to its delivery to the SCV. More experiments will be required to test this hypothesis.

## The SCV and the mitochondria are linked by intermembrane tethers

*S.* Typhimurium can be located within its vacuolar compartment (i.e. the SCV) or, after breaking from its vacuole, within the host cell cytosol. However, itaconate can only be

delivered to *Salmonella* located within the SCV[6]. Molecular transport mechanisms from the mitochondria to other vesicular compartments mediated by mitochondria-derived vesicles or involving direct contact between the recipient organelle and the mitochondria are well documented[55–59]. Therefore, to facilitate the delivery of itaconate to the SCV, RAB32 and/or LRRK2 may coordinate the formation and/or fusion of vesicle transport intermediates or may facilitate the association between the mitochondria and the SCV. Consistent with the latter, we have previously shown repeated contacts between the mitochondrial network and the SCV when observed by live time-lapse fluorescence microscopy[6]. To gain insight into the RAB32/LRRK2 coordinated transport mechanism we used cryo-electron tomography (cryo-ET) assisted by cryo-fluorescence microscopy (cryo-FM), and cryo-focused ion beam (cryo-FIB) milling, to visualize the SCV-mitochondria interface (Fig. 4a–c) (Video S1). HeLa cells stably expressing GFP-tagged IRG1 (Fig. 4 a–k) or bone marrow derived macrophages (BMDM) obtained from C57BL/6 mice (Fig. 4l–p) were infected with a *S.* Typhi encoding an mCherry-based itaconate biosensor. Guided by cryo-FM images (as shown in Fig. 4a), we used cryo-FIB milling to generate thin lamellae (<200 nm thickness) that contain bacteria that had been exposed to itaconate as indicated by the fluorescence associated with the biosensor (Fig. 4b and 4c). Cryo-ET imaging of the thin lamellae showed that by 1 hr after infection, a substantial proportion of the SCVs were seen in close association with the mitochondria in both HeLa (Fig. 4d–4k) and BMDM cells (Fig. 4l–p) (Extended Data Fig. 6). By 3 hs post infection, the majority of the SCVs were observed in close contact with the mitochondria. Importantly, the membranes of the SCVs and mitochondria were observed in close apposition, often extended over relatively long distances (Fig. 4d and 4g, and 4q). The average distance between the membranes in both HeLa and BMDM cells was ~16 nm, although in certain areas the distance was as close as ~10 nm (Fig. 4r). These observations are in keeping with reported distances between the mitochondria and other cellular organelles with which they engage in close interactions[60–62]. Notably, the interface showed the presence of tethers linking the SCV and the mitochondrial membranes (Fig. 4d–p). The tethers were abundant in both HeLa and BMDM cells, were closely spaced and distributed throughout the area of intermembrane-contact often arranging in clusters (Fig. 4f, 4j, 4k, 4o, 4p, 4s and Extended Data Fig. 7) (Video S1). Sub-tomogram averaging of the intermembrane tethers showed a continuous structure linking the two membranes (Fig. 4t). The tethers had an average length of 15 nm and average width of 4 nm. In addition, specific densities were observed that seem to anchor the tethers to each of the membranes (Fig. 4t). After submission of this manuscript, tethers linking the SCV to the endoplasmic reticulum were reported[63]. The relationship, if any, between these structures is unknown but since they link the SCV to different organelles, they are likely to be different. In keeping with the deleterious effect of itaconate, the appearance of *S.* Typhi contained within SCVs in close association with mitochondria was noticeably different at 1 and 3 hours after infection. At 1 hr after infection *S.* Typhi exhibited a smooth cytoplasm and a well-defined bacterial envelope, and no discernable differences were detected in their appearance whether they were in close association to mitochondria or not (Extended Data Fig. 6). However, by 3 hs after infection bacteria in close proximity to mitochondria appeared visibly altered, with pleiomorphic appearance and non-discernable membranes (a likely sign of bacterial death), which was more obvious in the case of BMDMs (Fig. 4l and Extended Data Fig. 6). The differences in bacterial morphology correlated with the

drop in colony forming unit (CFU) counts observed within the two time points (Extended Data Fig. 8a), as well as with the increased biosensor activity detected 3 hs post infection (Extended Data Fig. 8b and 8c). These observations are consistent with the notion that the close association of the SCV and the mitochondria results in itaconate delivery and bacterial death.

### LRRK2 is required for SCV-mitochondria association

To investigate the potential role of RAB32 and LRRK2 in the organization of the SCV-mitochondria interface we examined by cryo-FIB milling and cryo-ET, BMDMs obtained from C57BL/6 (parental), *Lrrk2*$^{-/-}$, or BLOC3 (the exchange factor for RAB32)-defective mice, that had been infected with wild-type *S.* Typhi. We also examined BMDMs from C57BL/6 mice infected with a *S.* Typhi strain expressing the *S.* Typhimurium T3SS effector GtgE, which with its protease activity specifically targets RAB32. We found that the absence of BLOC3 or the expression of GtgE in *S.* Typhi did not detectably alter the organization of the SCV-mitochondria interface as areas of close contact and the presence of tethers linking the two membranes were readily observed (Fig. 5a–h, Fig. 5o, and Extended Data Fig. 9). However, in keeping with defects in the delivery of itaconate observed in these cells[6] (Fig. 5p, 5q, Extended Data Fig. 8e and 8g), *S.* Typhi contained within the SCVs of BMDMs from BLOC3-deficient mice exhibit a normal cytoplasm and envelope architecture (Fig. 5e–h and Fig. 5r). Similarly, *S.* Typhi expressing the T3SS effector *gtgE* contained within SCVs of BMDMs from C57BL/6 mice exhibit a normal appearance (Extended Data Fig. 9). Notably, these bacteria displayed fully assembled T3SS injectisomes deployed at the interface between the SCV and the mitochondria (Fig. 6), in keeping with the ability of these bacteria to modulate the mitochondria-SCV interactions through the delivery of T3SS effectors. These results indicate that, while RAB32 is required for the efficient delivery of itaconate[6], it is not required for the establishment of the close association between the SCV and mitochondria.

In contrast, the proportion of close contacts between the SCV and the mitochondria in BMDMs obtained from *Lrrk2*$^{-/-}$ mice was significantly reduced (Fig. 5i–5o). Relative to C57BL/6 BMDMs, a much-reduced proportion of the SCVs were seen in close apposition to mitochondrial membranes (Fig. 5o). Furthermore, in the rare occasions of SCVs located in close association with the mitochondria, no tethers linking the two compartments were apparent in the *Lrrk2*$^{-/-}$ BMDMs (Fig. 5i–5n). These observations indicate that LRRK2 is required for the establishment of a close association between the SCV and the mitochondria.

## Discussion

We have shown here that the PD-associated kinase LRRK2 plays a central role in a Rab32-dependent cell intrinsic mechanism that controls *Salmonella* replication by facilitating the delivery of the antimicrobial compound itaconate to the SCV. We have previously shown that Rab32 forms a complex with aconitate decarboxylate 1 (IRG1), which synthesizes itaconate from mitochondrial precursors. Here we have shown that LRRK2 scaffolds the formation of this complex. Consistent with this hypothesis, in the absence of LRRK2, formation of the Rab32-IRG1 complex was impaired as was the delivery of itaconate to

the SCV, although the total synthesis of itaconate was unaffected. These results therefore suggest that LRRK2 facilitates the localized synthesis of itaconate at the mitochondria-SCV interface (see below), which is presumably essential for its delivery to the SCV.

How itaconate is delivered into the SCV and how LRRK2 facilitates this process are unclear although our results indicate that the formation of a close interface between the SCV and the mitochondria is essential for this process. Using cryo-ET aided by cryo-FIB milling we observed that the SCV and the mitochondria establish a very close association, with their membranes visibly in close apposition (~15 nm), often over a relatively long span. The close association between the SCV and the mitochondria is maintained by the presence of abundant tethers that linked these two compartments. Sub-tomogram averaging of the tethers revealed a well-defined density ~15 nm in length with domains anchoring the structure to the two apposed membranes. Consistent with the notion that the close of association of these compartments results in itaconate delivery and bacterial death, we observed that SCVs tethered to the mitochondria harbor bacteria with altered morphology characterized by pleiomorphic appearance and non-discernable membranes, features usually associated with dead bacteria.

Importantly, the close interaction between the SCV and mitochondria was not observed in LRRK2-defficient cells. Even in the rare occasions where the SCV and the mitochondria were observed in proximity to one another, no tethers were apparent. In contrast, the tethering of the SCV to the mitochondria was readily observed in cells deficient in BLOC3 (the Rab32 exchange factor), as well as in cells infected with an *S.* Typhi strain encoding the *S.* Typhimurium T3SS effector *gtgE*, and thus endowed with the ability to neutralize Rab32. These observations indicate that Rab32 is dispensable for the docking of the SCV to the mitochondria although it is essential for the delivery of itaconate to the SCV. In contrast, our results indicate that LRRK2 is required for both, the localized synthesis of itaconate and the close association of the SCV with the mitochondria.

How LRRK2 may coordinate these activities is unclear but it is likely that its kinase activity coupled to its ability to scaffold protein complexes afforded by its domain architecture are likely central to these functions. For example, it has been reported that LRRK2 can interact with the tricarboxylate transporter SLC25A[50–52], which most likely transports the mitochondrially-synthesized precursor cis-aconitate out of the mitochondrial matrix so that it can be converted to itaconate by IRG1. Therefore, we hypothesize that the ability of LRRK2 to interact with SLC25A1, Rab32, and IRG1 ensures the synthesis of itaconate at the mitochondria-SCV interface. This localized synthesis must be essential for its delivery to the SCV lumen since we have previously shown that cytosolic *Salmonella* (i. e. those that are not within the SCV) are not exposed to itaconate[6]. In addition, LRRK2 has been shown to interact with the microtubular network and myosin Va[52,64–66], which in turn may facilitate the docking of the SCV to the mitochondrial network (Extended Data Fig. 10). In fact, LRRK2 has been recently implicated in the regulation of the tethering of mitochondria to the endoplasmic reticulum[67]. More experiments will be required to test these hypotheses.

Taken together, the results presented here link the PD-associated kinase LRRK2 to a cell-intrinsic host defense mechanism against important bacterial pathogens. The most common

LRRK2 mutation associated with PD is LRRK2$^{G2019S}$, which results in a constitutively active kinase[68,69]. Since this mutation has also been associated with increased resistance to microbial infections including *Salmonella*[34,35], these observations provide a plausible pathway through which the LRRK2$^{G2019S}$ allele may have been selected in the human population, and constitute an example of how the evolutionary arms race between pathogens and host can shape human physiology.

## Methods

### Bacterial strains

All *Salmonella enterica* strains used in these studies are listed in Extended Data Table 1 and are derived from the wild-type *Salmonella enterica* serovar Typhi strain ISP2825[70], or serovar Typhimurium strain SL1344[71]. All mutant strains were constructed by allelic exchange as previously described[72] using the *E. coli* β−2163 Δ*nic35* as the conjugative donor strain[73]. All *Salmonella* strains were routinely cultured in LB broth containing 0.3 M NaCl at 37°C, conditions that stimulate the expression of the type III secretion system encoded within the pathogenicity island 1[74].

### Reagents and antibodies

Lipofectamine 2000 (Invitrogen), Nano-Glo Luciferase Assay Kit (Promega), puromycin and blasticidin (GIBCO), anti-FLAG M2 affinity gel (Sigma), and itaconic acid (Sigma), were purchased from the indicated sources. Mouse monoclonal antibodies against FLAG (Sigma, F1804; 1:2000), Alexa 594-conjugated anti-rabbit (Thermo Fisher Scientific, #A-11012), rabbit polyclonal antibodies against β-actin (Sigma, A2066; 1:3000), GFP (Invitrogen, A6455; 1:5000), IRG1 (Abcam, ab222411; 1:1000), LRRK2 (Abcam, ab133474; 1:1000), phospho-LRRK2 S935 (Abcam, ab133450; 1:1000), and *S.* Typhi (Sifin Diagnostics, #TS160S; 1:10000) were purchased from the indicated sources and used at the indicated dilutions.

### Plasmid construction

All plasmids used in this study and their sources are listed in supplementary Extended Data Table 2. Plasmids were constructed by the Gibson assembly strategy[75] and were verified by DNA sequencing.

### Cell culture and bacterial infections

Raw264.7, DC2.4, HeLa, and HEK293T cells as well as knockout derivatives were cultured in Dulbecco's modified Eagle medium (DMEM, GIBCO) supplemented with 10% Fetal Bovine Serum (FBS) at 37°C with 5% $CO_2$ in a humidified incubator. Cell lines were grown overnight in 24-well plates, 100 mm, or 150 mm dishes. Overnight cultures of the different bacterial strains were diluted 1/20 into fresh LB broth containing 0.3 M NaCl and further grown to an $OD_{600}$ of 0.9. Cell lines were infected with the different bacterial strains at the multiplicities of infection (MOI) indicated in the figure legends. One hour post infection, cells were washed with Hank's balanced salt solution (HBSS) and treated with gentamicin (100 μg/ml) for 1 hr to kill extra-cellular bacteria. Cells were then washed and cultured in

medium with low concentration gentamicin (10 μg/ml) for the times indicated in the figure legends.

### Generation of CRISPR/Cas9 edited cell lines

Generation of CRISPR/Cas9 edited cell lines was carried out as described previously following standard protocols[76,77]. Briefly, double-stranded oligonucleotides corresponding to mouse or human LRRK2 were cloned into the lenti-CRISPR-V2 vector and co-transfected with the packaging plasmids into HEK-293T cells. Two days after transfection, the viruses were harvested and used to infect Raw264.7, DC2.4, or HEK293T cells. The virally transduced cells were selected in culture media containing puromycin for 5 days and the isolated clones were screened by PCR and sequencing, or by Western blot to identify knockout cells. The nucleotide sequence of the guide RNAs and primers used to construct the different cell lines are listed in Extended Data Table 3.

### Generation of stable cell lines

DC2.4 cells stably expressing FLAG-tagged RAB32 have been described previously[6]. Raw264.7 parental or *Lrrk2*$^{-/-}$ cells expressing FLAG-RAB32 were generated through viral transduction and blasticidin selection. Briefly, transducing viruses were produced by co-transfecting into HEK-293T cells plasmids encoding FLAG-tagged RAB32 along with the packaging plasmids. Two days after transfection, viruses were harvested and used to infect Raw264.7 and DC2.4 cells. Transduced cells were selected with puromycin (for DC2.4 cells) or blasticidin (for Raw264.7 parental or *Lrrk2*$^{-/-}$ cells) for at least 5 days and resistant cells were tested for the expression of FLAG-tagged RAB32.

### Preparation of mouse BMDMs.

Mouse bone marrow-derived macrophages (BMDMs) were obtained from C57BL/6 or *Lrrk2*$^{-/-}$ mice as previously described[6]. Briefly, femurs and tibias from the indicated mice were flushed with PBS and single-cells suspensions were obtained by passage through a 70 μm cell strainer and centrifugation. Cell pellets were resuspended in DMEM medium containing L-929-conditined medium and plated in tissue culture plates.

### Co-immunoprecipitation and immunoblotting analyses

HEK-293T cells were transiently transfected with plasmid DNAs encoding the indicated proteins or empty vectors (as indicated in the figure legends) using the Lipofectamine 2000 reagent (Invitrogen) following the manufacturer's instruction. Twenty-four hs after transfection, cells were either lysed or infected with *S.* Typhimurium Δ*sopD2* Δ*gtgE* at a MOI of 5 and then lysed in 1 ml lysis buffer [20 mM Tris-HCl (pH7.4), 150 mM NaCl, 1 mM EDTA, 1% NP-40] containing protease and phosphatase inhibitors for 15 min on ice. The cell lysates were centrifuged at 14000 g for 15 min at 4°C, supernatants were collected, mixed with prewashed anti-Flag M2 agarose affinity gel (Sigma), incubated for 3 hs or overnight at 4°C. Beads were washed four times with cell lysis buffer containing 0.5 M NaCl and mixed with sample buffer. Eluted proteins were separated on 10% SDS-PAGE, transferred onto nitrocellulose membranes and processed for immunoblot analyses with the different primary antibodies (see figure legends) and with DyLight conjugated

secondary antibodies [emission 800 nm (ThermoFisher Scientific, Waltham, MA, USA). Blots were finally visualized on a LI-COR Odyssey imaging system (Lincoln, NE, USA). Where indicated, the intensity of the bands was quantified with the Odyssey v3.0 software package (Image Studio Lite LI-COR Biosciences). Stable Raw264.7 parental or *Lrrk2*$^{-/-}$ cells expressing FLAG-RAB32 and stable DC2.4 cells expressing FLAG-RAB32 were seeded onto 150 mm dishes overnight, cells were then infected with *S.* Typhimurium Δ*sopD2* Δ*gtgE* at the MOI indicated in the Figure legends or treated with LPS for the indicated times also as indicated in the figure legends. After infection, cells were subjected to co-immunoprecipitation and immunoblotting analyses as described above.

## Mitochondria isolation and protease protection assay

Raw264.7 parental and *Lrrk2*$^{-/-}$ cells, or DC2.4 cells stably expressing FLAG-RAB32 were treated with LPS (200 ng/ml) for 18 hs to induce the expression of IRG1. After treatment, cells were collected and centrifuged at 800 × g for 10 min at 4°C, cells were then washed with ice-cold PBS and lysed in 1 mL homogenization buffer (10 mM Tris-HCl [pH 7.4], 2 mM MgCl2, 10 mM KCl, and 250 mM sucrose) by 10 passages through a 25-gauge needle using a 1-mL syringe. After lysis, 50 μl of whole cell lysate was saved for further analysis. The homogenate was then centrifuged at 500 × g for 10 min at 4℃, the supernatant was further centrifuged at 5000 × g for 10 min at 4℃ to precipitate mitochondria, which were subsequently washed 2 times in homogenization buffer. After centrifugation at 5000 × g for 10 min at 4℃, the mitochondria pellets were subjected to the following treatments: (1) resuspended in 500 μl of homogenization buffer and incubated on ice for 30 min (untreated mitochondria); (2) resuspended in 500 μl of homogenization buffer containing 50 μg/ml of proteinase K and incubated on ice for 30 min (surface-exposed OMM proteins' digestion); (3) resuspended and incubated with 500 μl of 0.1% (v/v) Triton X-100 in homogenization buffer on ice for 20 min (no proteinase K added); and (4) resuspended and incubated with 500 μl of 0.1% (v/v) Triton X-100 in homogenization buffer on ice for 20 min and then incubated with 50 μg/ml of proteinase K on ice for further 30 min. The pellets were incubated with 2 mM PMSF on ice for 10 min to stop the activity of proteinase K and the mitochondria were then collected by centrifugation at 5000 × g for 10 min at 4°C and lysed in NP-40 lysis buffer as described above and analyzed by Western blots with antibodies directed to IRG1, the FLAG epitope (present in RAB32), LRRK2, cytochrome c and COX4 (as compartment markers).

## Luciferase reporter assays

Overnight cultures of the different *Salmonella* strains carrying a plasmid encoding an itaconate nanoluciferase-based biosensor were diluted 1/20 in LB broth containing 0.3 M NaCl and grown until an $OD_{600}$ of 0.9. The different mammalian cell lines or BMDMs were cultured overnight in 24-well plates and infected with the different *Salmonella* strains with the MOI and infection times indicated in the figure legends. After infection, cells were lysed with PBS containing 0.1% sodium deoxycholate and the levels of nanoluciferase were then measured using a BioTek Gen5 microplate reader (Agilent).

## DNA-PAINT super-resolution microscopy

**Materials.—**Cy3B-modified DNA oligonucleotides were custom-ordered from IDT. Sodium chloride 5 M (cat: AM9759) were obtained from Ambion. Ultrapure water (cat: 10977–015) was purchased from Invitrogen. μ-Slide 8-well chambers (cat: 80807) were purchased from ibidi. Methanol (cat: 9070–05) was purchased from J.T. Baker. Glycerol (cat: 65516–500ml), protocatechuate 3,4-dioxygenase pseudomonas (PCD) (cat: P8279), 3,4-dihydroxybenzoic acid (PCA) (cat: 37580–25G–F), and (+−)-6-hydroxy-2,5,7,8- tetramethylchromane-2-carboxylic acid (Trolox) (cat: 238813–5 G) were ordered from Sigma. Phosphate Buffered Saline (PBS) pH 7.2 (cat: 10010–023) was purchased from Gibco. Paraformaldehyde (cat: 15710) and glutaraldehyde (cat: 16219) were obtained from Electron Microscopy Sciences. Bovine serum albumin (cat: 001–000–162) was ordered from Jackson ImmunoResearch. Triton X-100 (cat: T8787–50ML) was purchased from Sigma Aldrich. Monoclonal antibodies against Cox IV (used: 1:300) (cat: 4850) were purchased from Cell Signaling. Antibodies against Flag-Tag (host: rabbit) (cat: 740001) (used: 1:500) were ordered from Thermofisher Antibodies against M45-Tag[78] (host: mouse) (generated in house from a hybridoma obtained from Pat Hearing[78]) (used: 1:100). DNA labeled Nanobodies against GFP were obtained from Massive Photonics (dilution 1:300). Secondary antibodies anti-rabbit (cat: 711–005–152) (used in a 1:300 dilution), were purchased from Jackson ImmunoResearch.

**Imaging Buffer.—**The imaging buffer (1xPBS, 500mM NaCl) was supplemented with 1× Trolox, 1× PCA and 1× PCD (see paragraph below for details).

**Trolox, PCA and PCD.—**100× Trolox: 100 mg Trolox, 430 μl 100 % Methanol, 345 μl 1M NaOH in 3.2 ml $H_2O$. 40× PCA: 154 mg PCA, 10 ml water and NaOH were mixed and pH was adjusted 9.0. 100× PCD: 9.3 mg PCD, 13.3 ml of buffer (100 mM Tris-HCl pH 8, 50 mM KCl, 1 mM EDTA, 50 % Glycerol). All preparations were stored at −20 °C.

**Antibody conjugation.—**Antibodies were conjugated to DNA-PAINT docking sites via DBCO-PEG2-succinimidyl ester chemistry as previously reported[79].

**Cell culture, fixation, and antibody labeling.—**HeLa cells stably expressing IRG1-GFP were seeded on 8-well glass coverslips at ~30,000 cells/well. Alternatively, HEK-293T cells were transiently transfected with plasmid DNAs encoding GFP-tagged LRRK2, FLAG-tagged RAB32, and M45-tagged Irg1 using the Lipofectamine 2000 reagent (Invitrogen) following the manufacturer's instruction. Cells were imaged 24 hs after transfection. In all cases, cells were fixed with 3 % formaldehyde, 0.1 % glutaraldehyde for 15 min, and after rinsing four times with 1× PBS for 30 s, 60 s, and twice for 5 min, samples were blocked and permeabilized with 3 % BSA and 0.25 % Triton X-100 for 2 hs. Then, samples were incubated with primary antibodies and GFP Nanobodies in a solution with 3 % BSA and 0.1 % Triton X-100 at 4 °C overnight. Cells were washed three times (5 min each) with 1× PBS. Next, they were incubated with labeled secondary antibodies (1:200 dilution) in a solution with 3 % BSA and 0.1 % Triton X-100 at room temperature for 2 hs. Finally, samples were rinsed three times with 1× PBS before adding the imaging buffer solution.

**Super-resolution microscope.—**Fluorescence imaging was carried out on an inverted Nikon Eclipse Ti2 microscope (Nikon Instruments) with the Perfect Focus System, attached to an Andor Dragonfly unit. The Dragonfly was used in the BTIRF mode, applying an objective-type TIRF configuration with an oil-immersion objective (Nikon Instruments, Apo SR TIRF 60×, NA 1.49, Oil). A 561 nm (1W nominal) laser was used for excitation of the fluorophores. The beam was coupled to a multimode fiber going through the Andor Borealis unit reshaping the beam from a gaussian profile to a homogenous flat top. As dichroic mirror a CR-DFLY-DMQD-01 was used. Fluorescence light was spectrally filtered with an emission filter (TR–DFLY–F600–050) and imaged on a scientific complementary metal oxide semiconductor (sCMOS) camera (Sona 4BV6X, Andor Technologies) without further magnification, resulting in an effective pixel size of 108 nm. The power at the objective lens was ~10 % of the power set at the laser.

**Conditions to image Irg1 and CoxIV.—**First round of imaging was carried out using an Imager strand concentration of 170 pM (R4 - Imager) in imaging buffer imaging IRG1. 15,000 frames were acquired at 50 ms exposure time. The readout bandwidth was set to 200 MHz. Laser power (@561 nm) was set to 50 mW (measured before the back focal plane (BFP) of the objective), corresponding to ~1.5 kW/cm$^2$ at the sample plane. After imaging the sample was subsequently washed five times with 200 μL each with 1× PBS (on the microscope). Second round of imaging was carried out using an imager strand concentration of 1 nM (P1 - Imager) in imaging buffer imaging CoxIV. 15,000 frames were acquired at 50 ms exposure time. The readout bandwidth was set to 200 MHz. Laser power (@561 nm) was set to 50 mW (measured before the back focal plane (BFP) of the objective), corresponding to 1.5 kW/cm$^2$ at the sample plane.

**Conditions to image Irg1, Rab32, and LRRK2.—**Before DNA-PAINT imaging a diffraction limited image of mCherry expressed in *Salmonella* was acquired with an exposure time of 500 ms and a laser intensity (@561 nm) of ~200 W/cm$^2$. First round of imaging was carried out using an imager strand concentration of 500 pM (P1 - Imager) in imaging buffer imaging IRG1. 25,000 frames were acquired at 50 ms exposure time. The readout bandwidth was set to 200 MHz. Laser power (@561 nm) was set to 50 mW (measured before the back focal plane (BFP) of the objective), corresponding to ~1.5 kW/cm$^2$ at the sample plane. After imaging the sample was subsequently washed five times with 200 μL each with 1× PBS (on the microscope). The second round of imaging was carried out using an imager strand concentration of 330 pM (P3 - Imager) in imaging buffer imaging Rab32. 25,000 frames were acquired at 50 ms exposure time. The readout bandwidth was set to 200 MHz. Laser power (@561 nm) was set to 50 mW (measured before the back focal plane (BFP) of the objective), corresponding to ~1.5 kW/cm$^2$ at the sample plane. After imaging the sample was subsequently washed five times with 200 μL each with 1× PBS (on the microscope). The third and final round of imaging was carried out using an imager strand concentration of 330 pM (R2 - Imager) in imaging buffer imaging LRRK2. 25,000 frames were acquired at 50 ms exposure time. The readout bandwidth was set to 200 MHz. Laser power (@561 nm) was set to 50 mW (measured before the back focal plane (BFP) of the objective), corresponding to ~1.5 kW/cm$^2$ at the sample plane.

**Image processing and analysis.—**DNA-PAINT data was reconstructed, postprocessed (drift correction and alignment of imaging rounds) and rendered with the Picasso package[79].

**Sequence of the oligonucleotides used for DNA-PAINT imaging.**

| Name | 5' End | Sequence (5' → 3') | 3' End |
|---|---|---|---|
| GFP-Nanobody-5xR2 | NB | AAACCACCACCACCACCACCA | |
| GFP-Nanobody-5xR4 | NB | AACAACACACACACACACA | |
| 2nd Antibody-P1 (anti-mouse) | AB | TTATACATCTA | |
| 2nd Antibody-P1 (anti-rabbit) | AB | TTATACATCTA | |
| 2nd Antibody-P3 (anti-rabbit) | AB | TTTCTTCATTA | |
| Imager R2 | | TGGTGGT | Cy3B |
| Imager R4 | | TGTGTGT | Cy3B |
| Imager P1 | | TAGATGTAT | Cy3B |
| Imager P3 | | TAATGAAGA | Cy3B |

## Measurement of itaconic acid concentration

Measurement of itaconic acid concentration in BMDMs and HeLa cells expressing GFP-IRG1 was carried out as previously described [6]. Briefly, HeLa cells expressing GFP-IRG1 or differentiated BMDMs ($1\times10^6$ cells) obtained from C57BL/6, *Lrrk2*$^{-/-}$ or *Irg1*$^{-/-}$mice treated with LPS (100 ng/ml) for 24 hs were washed with 0.9% NaCl. Samples were then extracted with LCMS grade methanolacetonitrile-water at 50:30:20 (v/v/v) (1 ml per $10^6$ cells) and subjected to LCMS analysis as previously described [6].

## Mice

*Lrrk2*$^{-/-}$ mice on C57BL/6 background were purchased from Jackson Laboratory. *Irg1*$^{-/-}$ mice were derived from embryonic stem cells (*Irg1*$^{tm1a(KOMP)Wtsi}$) from the knockout mouse project repository (KOMP, University of California Davis)[80], and generously provided by M. Diamond, Washington University.

## Mouse infections

All animal experiments were performed according to protocols approved by Yale University's Institutional Animal Care and Use Committee (IACUC) under protocol number 2019–07858. Six- to ten-week-old, age- and sex-matched mice were used in all the experiments, which were conducted without blinding. The different *Salmonella* strains were cultured overnight and then diluted 1/20 in LB broth containing 0.3 M NaCl and grown until an $OD_{600}$ of 0.9, and animals were intraperitoneally infected with the doses indicated in the Figure legends. To measure bacterial loads in the spleens, four days after infection, mice were sacrificed, spleens were homogenized in 2 ml of PBS containing 0.1% sodium deoxycholate, and different dilutions were then plated on LB plates to determine CFU.

## Cryo-ET sample preparation

R1/4 carbon-foil 200 mesh gold cryo-EM grids (Quantifoil) were glow discharged, coated with 0.1 mg/ml poly-D-lysine for 1 hr, and disinfected with UV light inside a biosafety cabinet for 15–30 min. Cryo-EM grids were rinsed four times with sterile water and incubated with fully supplemented cell culture medium at 37°C under 5% $CO_2$ for >8 hs. HeLa cells stably expressing EGFP-tagged IRG1 or BMDMs obtained from C57BL/6, BLOC3, or LRRK2-deficient mice were seeded onto the pre-treated cryo-EM grids and allowed to grow on the grid surface overnight at 37°C under 5% $CO_2$. Overnight cultures of *S.* Typhi encoding an mCherry-based itaconate biosensor or expressing mScarlet were diluted 1/20 into fresh LB containing 0.3 M NaCl and further grown to an $OD_{600}$ of 0.9. The BMDMs were treated with LPS (200 ng/ml) for 3 hs prior to the infection, and then infected with the indicated bacterial strains at the multiplicities of infection (MOI) indicated in the figure legends. One hour post infection, cells were then washed three times with Hank's balanced salt solution (HBSS) and treated with gentamicin (100 μg/ml) for 1 hr to kill extra-cellular bacteria. Cells were then washed and cultured in medium with low concentration gentamicin (10 μg/ml) for the times indicated in the figure legends. Cryo-EM grids containing infected cells were incubated in fully supplemented medium containing 10% glycerol for ~ 1min to prevent the formation of crystalline ice. Excess medium was blotted away from the cryo-EM grid with filter paper from the backside and then immediately plunge frozen in liquid ethane using a gravity-driven homemade plunger apparatus.

## Correlative cryo-fluorescence microscopy and cryo-focused ion beam (cryo-FIB) milling

Vitrified specimens were clipped with cryo-FIB milling compatible autogrids (Thermo Fisher Scientific) and loaded to a Cryo-CLEM (Leica) microscope for fluorescence imaging at <−180°C. Using a 50 x cryo-objective lens, 6×6 Z-stacks (1 micrometer increment in the Z direction) that cover ~80% of the grid surface were collected with bright field and fluorescence channels at 488 and 561 nm. Using the "active extended depth of field" function in the Leica operating software LAS X, projection images of the z-stacks were generated and exported to a file format compatible with MAPS (Thermo Fisher Scientific) software to correlate fluorescence signals for cryo-FIB milling.

Cryo-FIB milling was performed using an Aquilos 2 FIB/SEM instrument (Thermo Fisher Scientific). Using the MAPS software, a low magnification SEM montage of the entire grid was acquired, and identifiable features (e. g. teared carbon films) were used to overlay the cryo-fluorescence image. Samples were sputtered with a metallic platinum for 15 seconds followed by a coating with a layer of organometallic platinum (Pt) for 25 seconds. Additional 15 seconds of sputtering with a metallic platinum was applied to prevent drifting during the milling due to charging effect. Precise locations for milling were determined by the fluorescence signals from the intracellular *S.* Typhi in X and Y directions. To preserve the target bacteria within the cryo-lamellae, specimens were milled only from the top gradually using gallium ion beam until the bacteria is identified in the SEM images. Once the desired features were found in SEM images, samples were thinned from the bottom to achieve lamellae with <~150 nm thickness. Lastly, the lamellae were sputtered with metallic platinum for 4 seconds.

### Cryo-ET data collection and reconstruction

The cryo-lamellae were imaged under a Titan Krios (Thermo Fisher Scientific) equipped with a Gatan K3 direct electron detector, a Volta phase plate (VPP), and an energy filter with slit width of 20 eV, using a target defocus of −1μm. Samples were also imaged under a Glacios (Thermo Fisher Scientific) microscope equipped with a Gatan K2 electron detector, with a target defocus of −6μm. The data collection package SerialEM[81] was used to collect 35 image stacks at a range of tilt angles between +51° to −51° (after adjusting for the milling angle), with 3° step size using the bi-directional scheme with a cumulative dose of ~70 $e^-/Å^2$. Each image stack containing 10–15 images were aligned using Motioncor2[82] and then assembled into the drift-corrected stacks by TOMOAUTO[83]. The drift-corrected stacks were aligned and reconstructed by IMOD[84] marker-dependent alignment using the Pt residues as fiducials.

### Subtomogram averaging

The subtomogram averaging package I3 (0.9.9.3) was used to average the intermembrane tethers and TTSS[85]. Intermembrane tethers and T3SS injectisomes were manually selected from the bind4 tomograms. For the tethers, we first recorded the coordinates of their vacuolar end and subsequently recorded the coordinates of their mitochondrial end. Similarly, we recorded two coordinates for each T3SS injectisome particle from their bacterial inner and outer membrane ends. Based on this selection strategy, the orientations of the tethers were estimated to facilitate the averaging process. For normalization, particles were extracted from the bin 1 tomograms and then rescaled to 4.556Å/pix. 3D refinements and classifications were performed iteratively from bin4, bin2, and bin1 particles until no further improvement was apparent. After iterative classifications, 456/493 tethers and 226/348 T3SS injectisomes were used for the final reconstructions. Only the tether density at the bin4 average map was segmented using the UCSF ChimeraX software[86] and mapped back into the original tomograms based on alignment values using a MATLAB-based in-house script. EMAN 2.9[87] was used to identify bacterial ribosomes shown in Figure 4 by the reference-based picking module, averaged to ~40Å resolution, and mapped back into the original tomograms using the map-back option in EMAN2.9[87].

### 3-dimentional rendering and visualization

Features of interest such as bacterial, vacuolar and mitochondrial membranes were semi-automatically segmented using the EMAN 2.9 segmentation tool[88]. The segmentation results were further polished with the Amira software (Thermo Fisher Scientific). Segmented volumes and mapped-backed average structures were visualized using UCSF ChimeraX[89]. The movie clip was generated using UCSF ChimeraX and edited in Keynote. IsoNet software[90] was used to denoise tomograms used in the main figures to increase image contrast.

### Statistical analysis

Unless indicated otherwise, all experiments were performed at least three times independently. Unpaired Student's *t* test was used for statistical analysis with GraphPad Prism Software version 9.0. Significance of mean comparison is annotated as follow: ns, not

significant; * $P$<0.05; ** $P$<0.01; *** $P$<0.001; **** $P$<0.0001. A $P$ value of < 0.05 was considered to be statistically significant.

## Extended Data

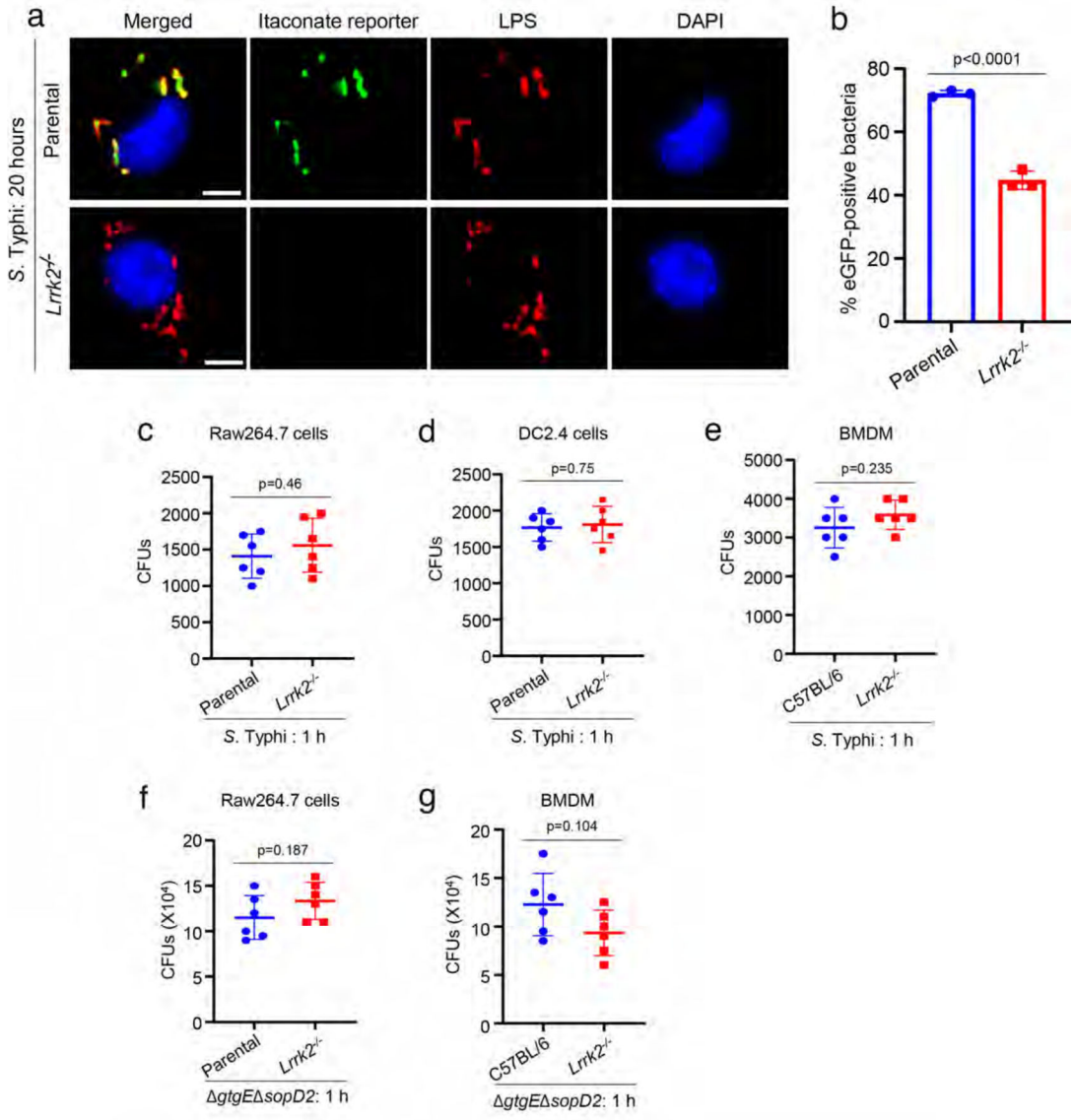


**Extended Data Fig. 1.**

**(a** and **b)** LRRK2 is required for efficient itaconate delivery to the *Salmonella*-containing vacuole. Parental (control) and *Lrrk2*$^{-/-}$ Raw264.7 cells were infected with *S.* Typhi (MOI = 6) encoding an eGFP-based itaconate biosensor and the number of cells expressing eGFP was determined 20 hours after infection. Each square and circle represents the mean of an individual experiment experiments in which at least 200 infected cells were examined (**b**). The *p* value (unpaired two-tailed Student's t test) of the indicated comparison is shown. Infected cells were fixed, stained with DAPI (blue) to visualize nuclei, and stained with an anti-*Salmonella* LPS antibody along with Alexa 594-conjugated anti-rabbit antibody

(red) to visualize all bacteria. Representative fields of infected cells are shown (**a**) (scale bar = 5 μm). (**c-g**) Absence of LRRK2 does not influence the uptake of *Salmonella* into phagocytic cells. Raw264.7 or DC2.4 parental (control) and *Lrrk2*$^{-/-}$ cells, as well as bone marrow-derived macrophages (BMDM) derived from C57BL/6 and *Lrrk2*$^{-/-}$ mice were infected with either wild-type *S.* Typhi (MOI = 6) or a *S.* Typhimurium Δ*gtgE* Δ*sopD2* mutant strain (MOI = 3) (as indicated) and the number of CFU was determined 1 hr after infection. Each square or circle represents the CFU in an independent measurement. The mean ± SD and *p* values (unpaired two-tailed Student's t test) of the indicated comparisons are shown.

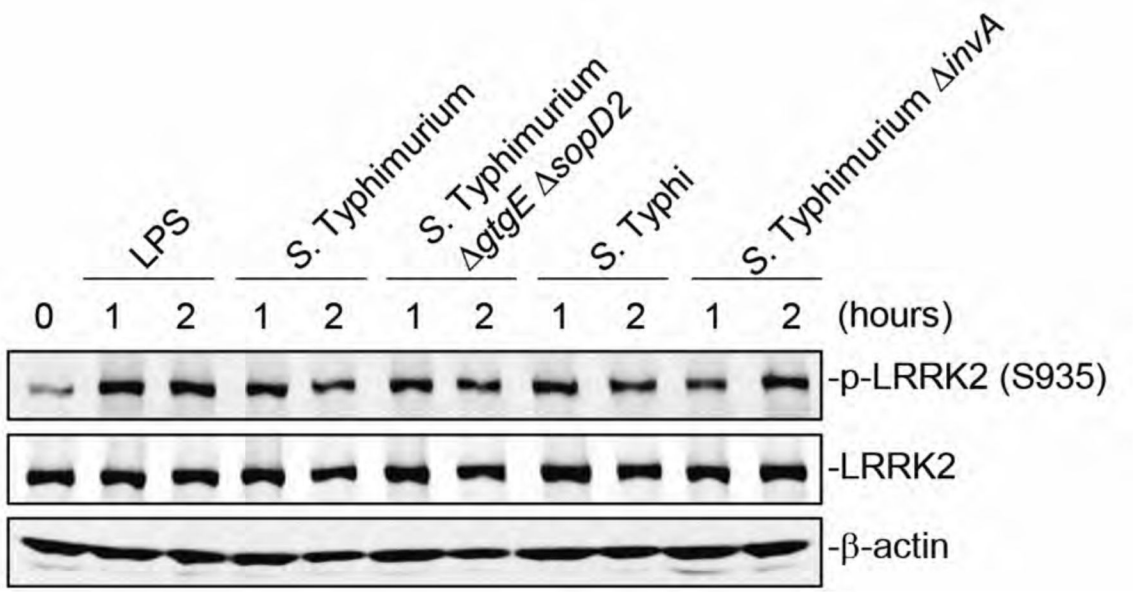


**Extended Data Fig. 2. *Salmonella* infection results in LRRK2 activation.**

DC2.4 cells were treated with LPS or infected with the indicated bacterial strains for the indicated times. The activation of LRRK2, assessed by its phosphorylation at S935, was then analyzed by immunoblotting with the indicated antibodies.

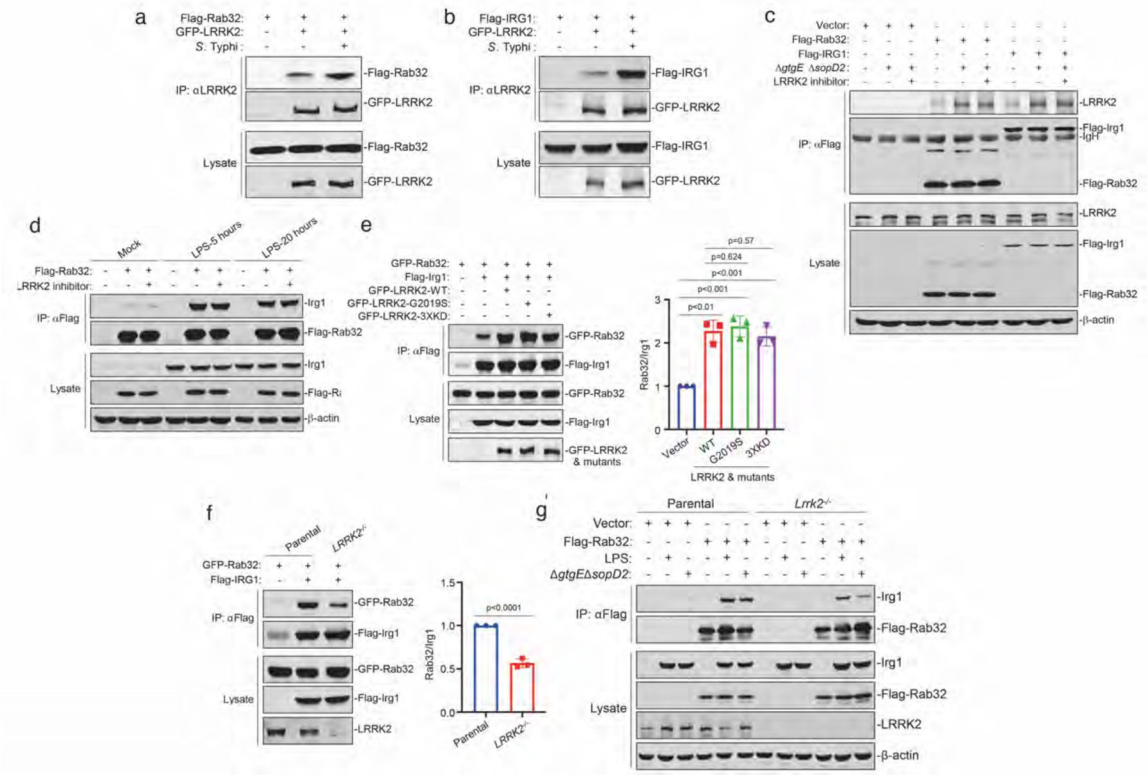


**Extended Data Fig. 3. LRRK2 scaffolds the formation of RAB32 and IRG1 complex.**

(**a** and **b**) LRRK2 interacts with RAB32 and IRG1. HEK293T cells were transiently co-transfected with a plasmid expressing GFP-LRRK2 and a plasmid expressing either FLAG-RAB32 (**a**) or FLAG-IRG1 (**b**). Twenty hours after transfection cells were infected with *S.* Typhi (MOI = 6) and 4 hs after infection, cell lysates were analyzed by immunoprecipitation and immunoblotting with antibodies against the FLAG epitope and GFP. (**c**-**e**) The kinase activity of LRRK2 is not required to form a complex with RAB32 and IRG1. (**c** and **d**) Raw264.7 (**c**) or DC2.4 (**d**) cells stably expressing FLAG-RAB32 or FLAG-IRG1 were pre-treated with the LRRK2 kinase inhibitor GSK2578215A for 90 min, infected with the *S.* Typhimurium Δ*gtgE* Δ*sopD2* mutant strain (MOI=3) (**c**) or treated with LPS (**d**). Eighteen hours after infection or 5 or 20 hs after LPS treatment, cell lysates were analyzed by immunoprecipitation and immunoblotting with the indicated antibodies. (**e**) HEK293T cells were transiently co-transfected with plasmids expressing GFP-RAB32, FLAG-Irg1, and the indicated forms of LRRK2: wild type (WT), kinase defective (3XKD = LRRK2K$^{1906A/D1994A/D2017A}$), and constitutively active (LRRK2$^{G2019S}$). Twenty hours after transfection, cell lysates were analyzed by immunoprecipitation and immunoblotting with the indicated antibodies. The quantification of the intensity of the RAB32 band relative to the intensity of the IRG1 band is shown in. Each circle, square, or triangle represents a measurement in an independent experiment. The mean ± SD and *p* values (unpaired two-tailed Student's *t* test) of the indicated comparisons are shown. (**f** and **g**) HEK293T parental or *LRRK2*$^{-/-}$ cells were transfected with GFP-RAB32 and FLAG-IRG1 for 20 hs. Cell lysates were then analyzed by immunoprecipitation with anti-FLAG and immunoblotting with anti-GFP antibody. The quantification of the intensity of the RAB32 band relative to the intensity

of the IRG1 band is shown (**f**). Each circle or square represents a measurement in an independent experiment. The mean ± SD and *p* values (unpaired two-tailed Student's *t* test) of the indicated comparisons are shown. (**g**) Raw264.7 parental or *Lrrk2*$^{-/-}$ cells stably expressing FLAG-RAB32 were left untreated, treated with LPS, or infected with *S.* Typhimurium Δ*gtgE* Δ*sopD2* mutant strain (MOI = 3) for 18 hs. Cell lysates were then analyzed by immunoprecipitation with anti-FLAG and immunoblotting with the indicated antibodies.

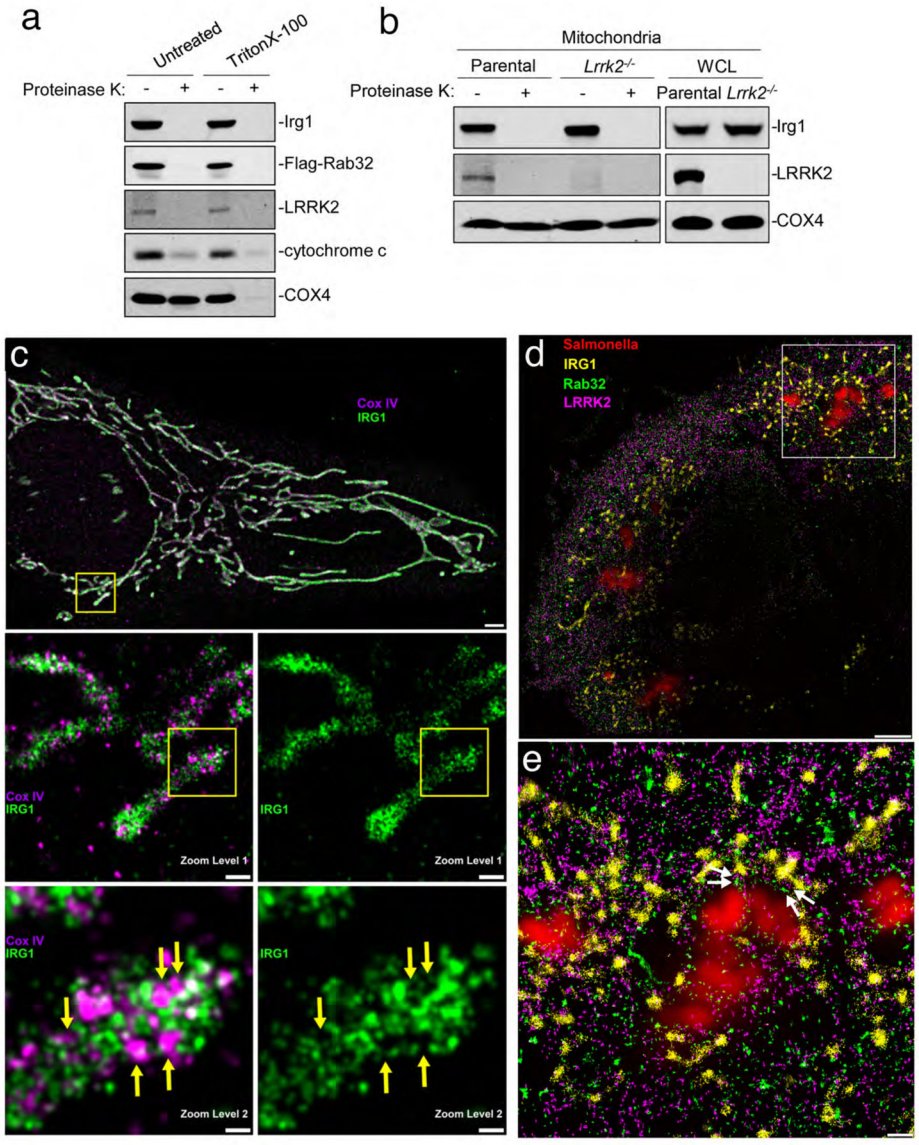


**Extended Data Fig. 4. Localization of LRRK2, RAB32, and IRG1. (a and b) LRRK2, RAB32, and IRG1are associated with the mitochondria accessible to protease digestion.**

DC2.4 cells stably expressing RAB32 **(a),** or DC2.4 parental (control) and *Lrrk2*$^{-/-}$ cells (b) were treated with LPS for 18 hs, mitochondria were purified and treated with proteinase K or left untreated, and subsequently analyzed by immunoblotting with the indicated antibodies. (**c**) Two color DNA-PAINT super-resolution image demonstrating that IRG1

does not co-localize with the mitochondrial matrix protein Cox IV. The top panel presents a HeLa cell expressing GFP-tagged IRG1 (green). Cells were fixed and stained with nanobodies to the GFP epitope, and primary and secondary antibodies to Cox IV (magenta). Nanobodies and secondary antibodies were labeled with a single stranded DNA oligomer acting as a docking site for DNA-PAINT super-resolution microscopy. First and second zoom levels show that Cox IV and IRG1 are spatially excluded from each other. The yellow arrows in zoom level two highlight examples of the spatial exclusion of Cox IV and IRG1. Scale bars 2 μm (top panel), 400 nm (zoom level 1) and 100 nm (zoom level 2). (**d** and **e**) Three-plex DNA-PAINT super-resolution image showing proximity of RAB32, LRRK2, and IRG1. (**d**) Hek293T cells expressing GFP-tagged LRRK2 (purple – DNA-PAINT), FLAG-tagged Rab32 (green – DNA-PAINT), and M45-tagged IRG1 (yellow – DNA-PAINT) were infected with *S.* Typhi carrying plasmid encoding an mCherry-based itaconate reporter (red – diffraction limited image). Cells were fixed and stained with nanobodies to the GFP epitope, and M45 and FLAG tags were labeled with primary antibodies and secondary antibodies conjugated to a single stranded DNA oligomer acting as a docking site for DNA-PAINT super-resolution microscopy. (**e**) The zoom in shows the spatial proximity of the three proteins in the proximity of S. Typhi expressing the itaconate reporter. The white arrows in the zoom-in highlight examples of the proximity cluster of the three proteins. Scale bars 5 μm (**d**), 1 μm (**e**).

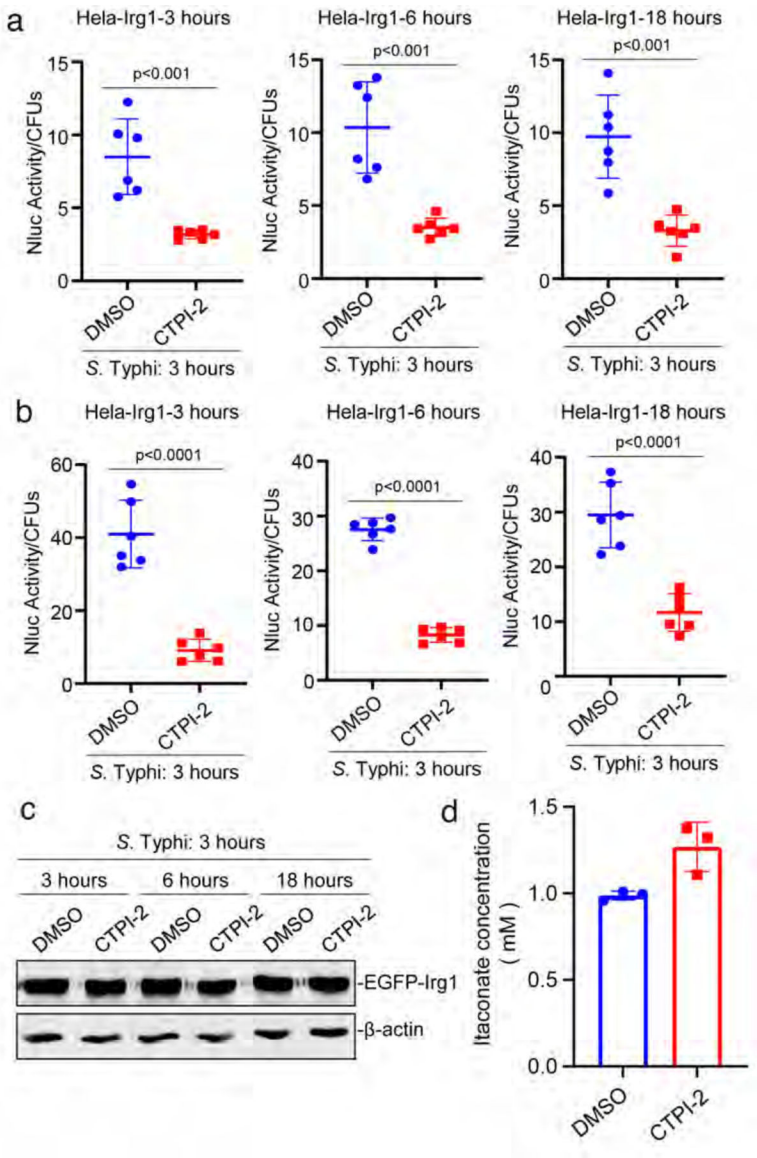


**Extended Data Fig. 5. Inhibition of the mitochondrial tricarboxylate transporter SLC25A1 impairs itaconate delivery to the *Salmonella*-containing vacuole.**

**(a** and **b)** HeLa cells stably expressing EGFP-tagged IRG1 were pre-treated with the SLC25A1 transporter inhibitor CTPI-2 for 3, 6, or 18 hrs (as indicated), and then infected with wild-type *S.* Typhi (MOI = 6) encoding a luciferase-based itaconate biosensor. The levels of luciferase activity in the cell lysates were then measured 3 hs after infection. Each circle or square represents a single luciferase measurement. The mean ± SD and *p* values (unpaired two-tailed Student's t test) of the indicated comparisons are shown. **(a)** and **(b)** show results of two independent experiments. (**c** and **d**) Inhibition of the mitochondrial tricarboxylate transporter SLC25A1 does not impair IRG1 expression or overall itaconate biosynthesis. (**c**) HeLa cells stably expressing EGFP-tagged IRG1 were pre-treated with the SLC25A1 transporter inhibitor CTPI-2 for 3, 6, or 18 hrs (as indicated), and then infected with wild-type *S.* Typhi (MOI = 6) encoding a luciferase-based itaconate biosensor as indicated in Extended Data Fig. 10. The levels of IRG1 3, 6 or 18 hours after CTPI-2

treatment were evaluated by western immunoblot with the indicated antibodies. (**d**) HeLa cells stably expressing EGFP-tagged IRG1 were pre-treated with the SLC25A1 transporter inhibitor CTPI-2 for 18 hrs, and the levels of itaconate were measured as indicated in Materials and Methods. Each square represents a single measurement and the mean and SD are shown.

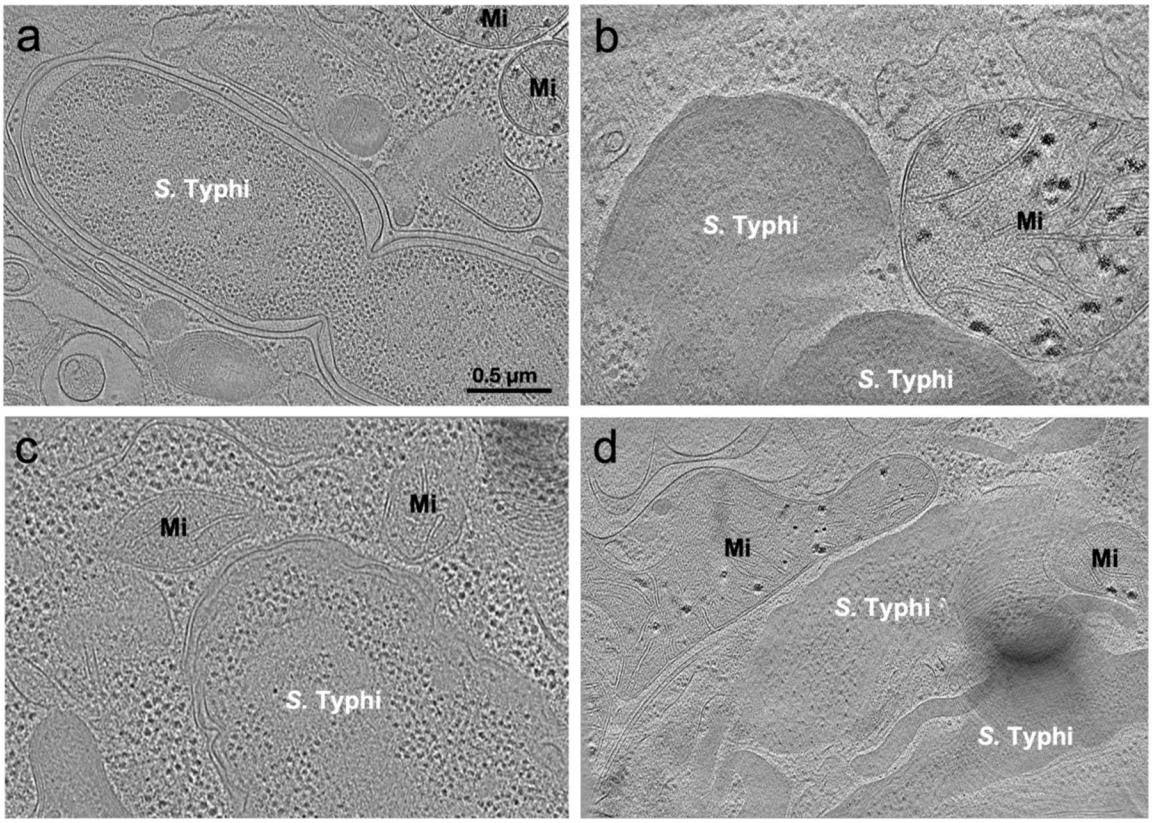


**Extended Data Fig. 6. Tomographic slices of S. Typhi infected cells at different times after infection.**

HeLa cells expression IRG1 (**a** and **b**) or BMDMs obtained from C57BL/6 mice (**c** and **d**) were infected with *S.* Typhi and 1 **(a** and **c**) and 3 (**b** and **d**) hrs after infection were processed for cryo-ET imaging. Shown are representative tomographic slices showing that the appearance of *S.* Typhi within cells over time. Bacteria within HeLa-IRG1 cells 1 hr after infection appear normal, with many ribosomes and an intact bacterial envelope. However, bacteria within HeLa-IRG1 cells 3 hs post-infection or within BMDMs at 1 and 3 hrs post infection exhibit altered morphology. Mi: mitochondria

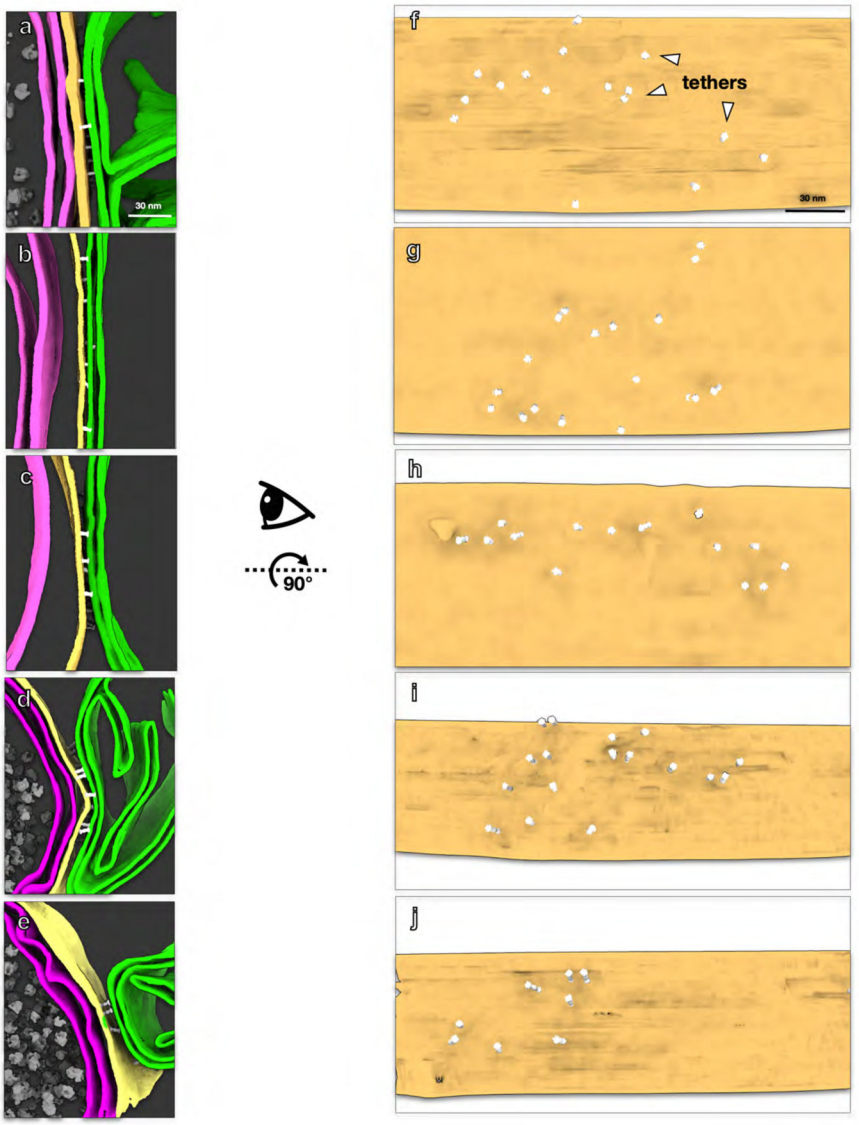


**Extended Data Fig. 7. Visualization of tethers at the SCV-mitochondria interface.**

(**a-e**) 3D renderings of the SCV-mitochondria interfaces shown in Figures 4f, 4j, 4k, 4o, and 4p, respectively. Magenta, yellow, and green represent bacterial, vacuolar, and mitochondrial membranes, respectively. Intermembrane tethers are depicted in white. Please refer to the main Figure 4 figure legend for experimental details. (**f-j**) Top-down views of the corresponding interfaces in Panels (**a-e**), revealing vacuolar membrane surfaces decorated with intermembrane tethers.

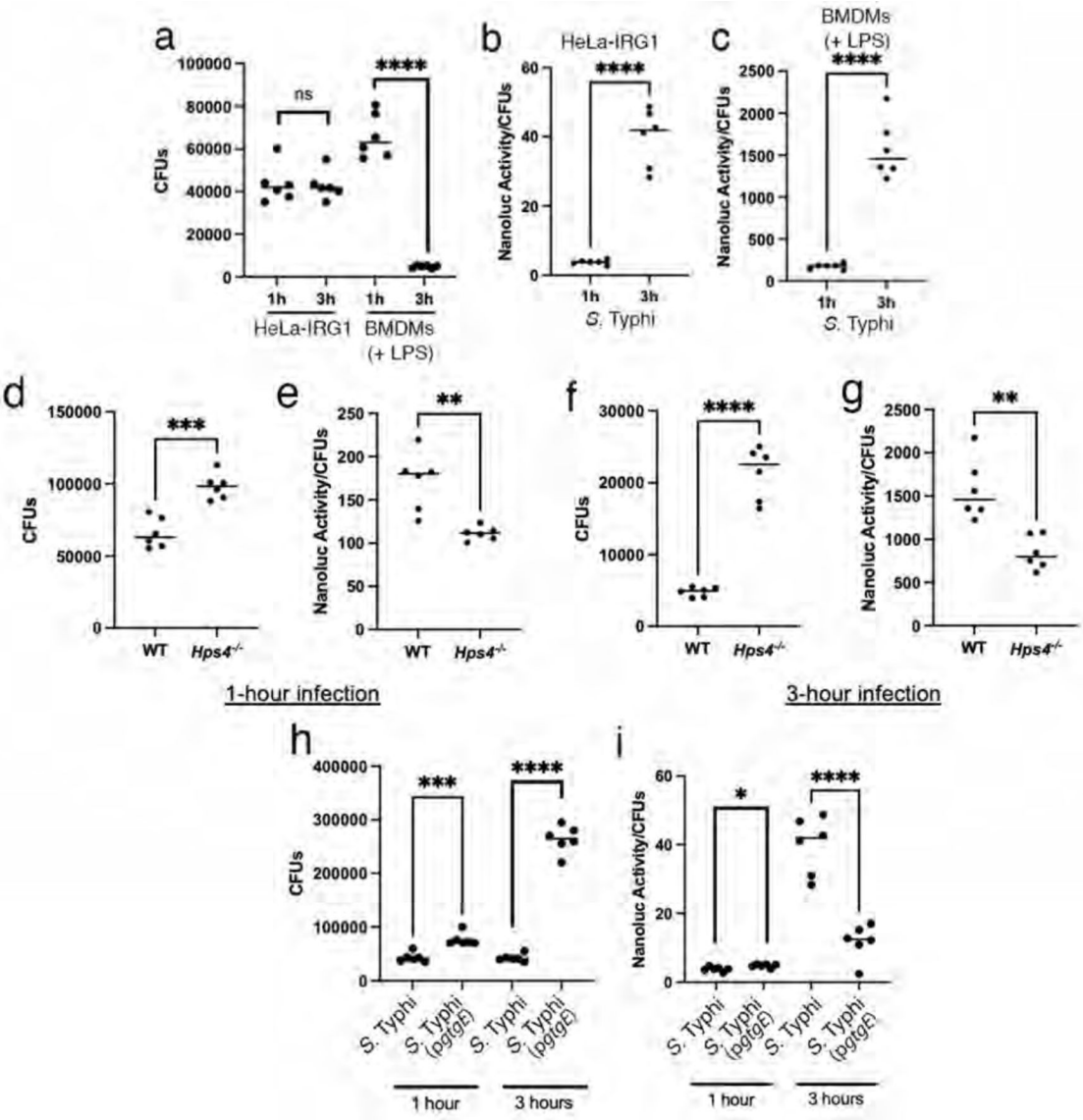


**Extended Data Fig. 8. Itaconate delivery and bacterial growth in cells used for cryo-ET analysis.**

(**a**) HeLa cells stably expressing IRG1 or BMDMs from C57BL/6 mice treated with LPS (200ng/ml) for 3 hours were infected with *S.* Typhi (MOI=10), and the number of CFU was determined 1 and 3 hrs after infection. Each circle represents the CFU in an independent measurement; the mean ± SEM of all the measurements and *p* values of the indicated comparisons (two-sided Student's t test) are shown. ns, not significant. ****p < 0.0001. (**b** and **c**) HeLa cells stably expressing IRG1 (**b**) or BMDMs from C57BL/6 mice treated with LPS (200ng/ml) for 3 hrs (**c**) were infected with *S.* Typhi (MOI=10) carrying a plasmid encoding the itaconate nanoluciferase biosensor. One and three hours after infection, the levels of nanoluciferase were measured in lysates of the infected cells. Each circle represents a single luciferase measurement. The mean ± SD and *p*-values of the indicated comparisons (two-sided Student's t-test) are shown. ****p < 0.0001. (**d-g**) BMDMs obtained from C57BL/6 (WT) or *Hps4*$^{-/-}$ were infected with *S.* Typhi (MOI = 10) carrying a plasmid encoding the itaconate nanoluciferase biosensor, and the number of CFU was determined

1 (**a**) or 3 (**c**) hs after infection. Alternatively, the levels of nanoluciferase were measured in lysates of the infected cells (**b** and **d**). Each circle represents the CFU in independent measurements (**a** and **c**) or a single luciferase measurement (**b** and **d**). Shown are the mean ± SEM of all the measurements; *p* values of the indicated comparisons (two-sided Student's t test) are shown. **p < 0.01 and ***p < 0.001, ****p < 0.0001. (h and i) Itaconate delivery and intracellular growth of *S.* Typhi expressing *gtgE* in cells used for cryo-ET analysis. (**h** and **i**) HeLa cells stably expressing IRG1 were infected with *S.* Typhi or *S.* Typhi- expressing *gtgE* (MOI=10) carrying a plasmid encoding the itaconate nanoluciferase biosensor. The number of CFU (**a**) or the level of luciferase activity (**b**) was determined 1 hour or 3 hours after infection. Each circle represents a single measurement. Values are the mean ± SEM of all the measurements and *p* values of the indicated comparisons (two-sided Student's t test) are shown. *$p < 0.05$, **$p < 0.01$, ***$p < 0.001$, ****$p < 0.0001$.

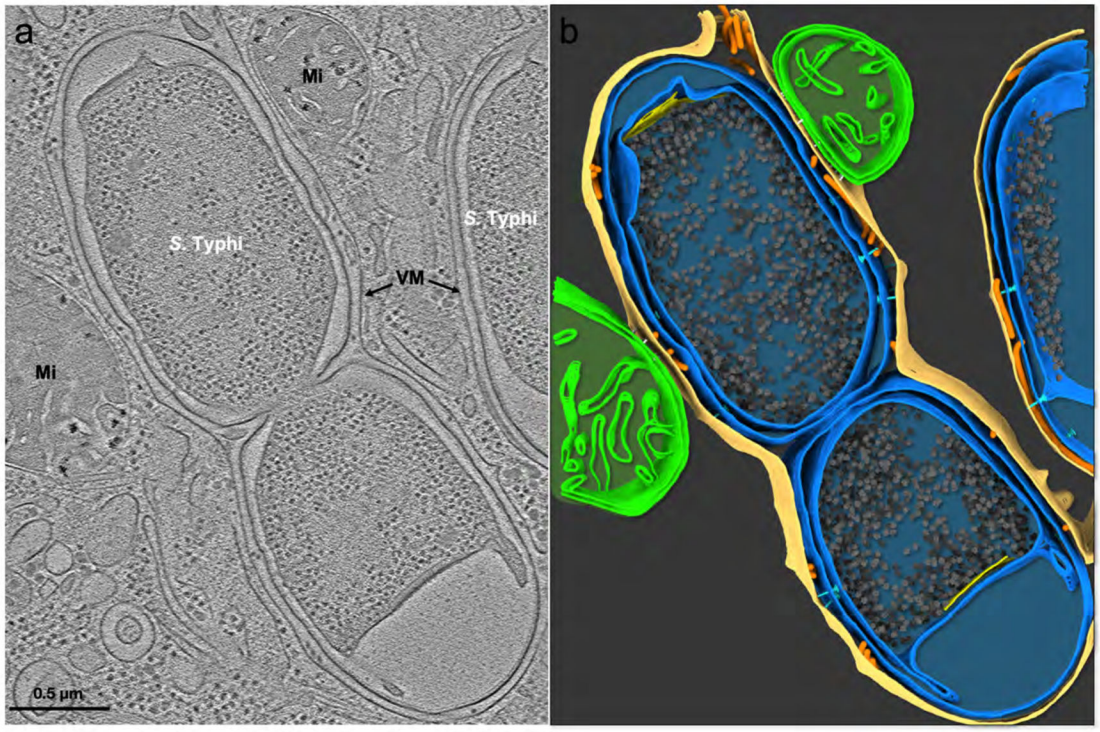


**Extended Data Fig. 9. Expression of the *S*. Typhimurium effector protein GtgE in *S*. Typhi does not prevent SCV-mitochondria association and tethering.**

(**a**) Tomographic slice showing *S.* Typhi strain expressing GtgE within its replication vacuole and surrounding mitochondria (Mi) intimately interacting with the vacuolar membrane (VM). (**b**) 3D-rendering of the tomogram shown in panel (**a**)(z=86 slices). Mitochondria is depicted in green, the SCV membrane in yellow, bacterial envelope in blue, inter membrane tethers in white, type III secretion machines in light blue, and bacterial ribosomes in grey (see close ups of the SCV-mitochondria interface in Fig. S14).

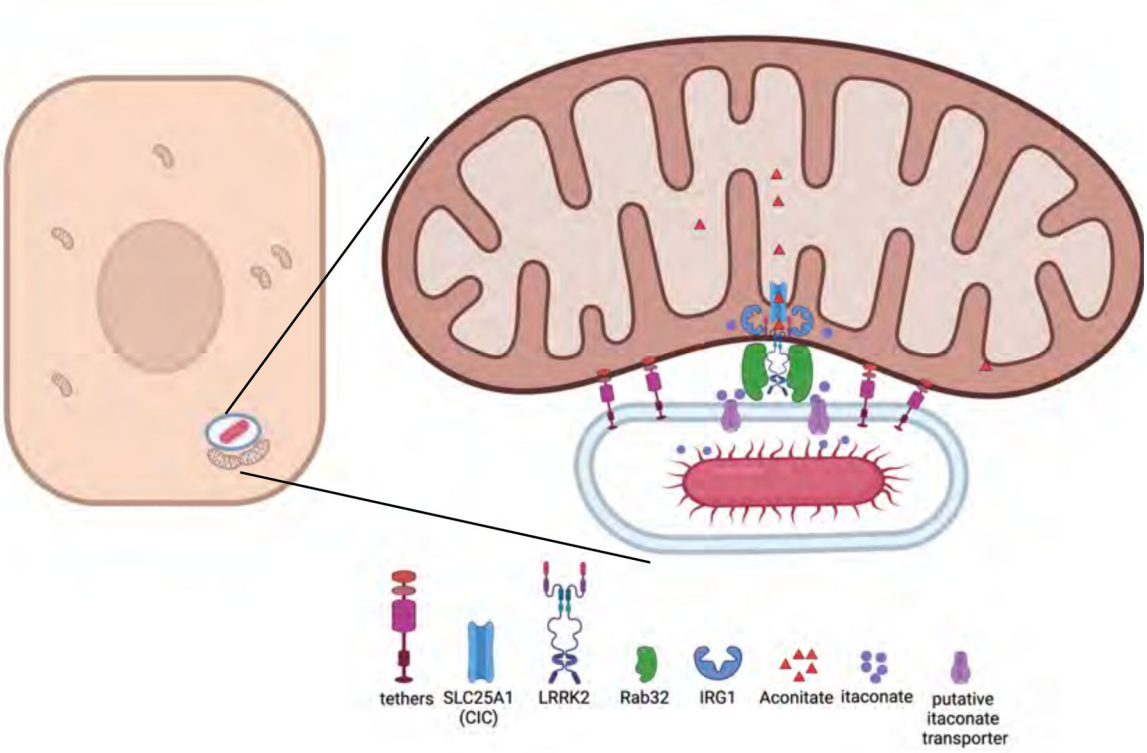


**Extended data Fig. 10. Model for the role of LRRK2 in itaconate delivery to the *Salmonella* containing vacuole.**

LRRK2 may coordinate the close apposition between the *Salmonella*-containing vacuole (SCV) and the mitochondria (not depicted in this model) as it has been proposed to do with other intracellular organelles (64). In addition, as depicted in this model, through its ability to scaffold a complex between RAB32, IRG1, and SLC25A1, LRRK2 may coordinate the localized synthesis of itaconate at the mitochondria/SCV interface.(generated with the help of Biorender (www.biorender.com).

## Extended Data Table 1.

List of bacterial strains used in this study

| Strain | Relevant genotype | Reference |
|---|---|---|
| *S.* Typhimurium SB300 | Mouse-passed wild-type *S.* Typhimurium SL1344 | PMID: 7015147 |
| *S.* Typhimurium SB2527 | Δ*gtgE* Δ*sopD2* | PMID: 26867181 |
| *S.* Typhi ISP2825 | Wild type | PMID: 26867180 |

## Extended Data Table 2.

List of plasmids used in this study

| Plasmid | Description | Reference |
|---|---|---|
| pSB6052 | pRK5-FLAG-RAB32 | PMID: 32703879 |
| pSB4657 | pEGFPC1-RAB32 | PMID: 32703879 |
| pSB6761 | Lenti-CMV-FLAG-RAB32 (blasticidin) | This study |
| pSB6053 | pRK5-FLAG-IRG1 | PMID: 32703879 |
| pSB6763 | pWSK-rpsm-scarlet | This study |

## Extended Data Table 3.

Primers used in the construction and screening of CRISPR/Cas9 genome edited cell lines

| Primer Name | Nucleotide Sequence |
|---|---|
| sg-mouse LRRK2 | 5’-GCATGTCTTTGTGGTGAAAG −3’ |
| sg-human LRRK2 | 5’-GCGATCCAAGGAACCCTTGG −3’ |
| mouse LRRK2-identification-Fw | 5’-ACGTAAGCAGATAGATCTCTGG −3’ |
| mouse LRRK2-identification-Rv | 5’-GCTCTCAACAGACTATCCTTTAC −3’ |
| human LRRK2-identification-Fw | 5’-AGAGAAGAAATGGAAAGTTTGC −3’ |
| human LRRK2-identification-Rv | 5’-CTACTTGCTATGAGGTTCTGC −3’ |

## Extended Data Table 4.

Summary of Cryo-ET data

| Sample | No. of tiltseries | Instrument and parameter | Pixel Size (Å/pixel) |
|---|---|---|---|
| WT HeLa infected with S. Typhi (1h) | 19 | Glacios, 200keV, K2 camera, −6 μm defocus | 3.827 |
| WT HeLa infected with S. Typhi (1h) | 19 | Titan Krios, 300keV, K3 camera, energy filter (20 eV), Volta phase plate (VPP) with −1 μm defocus | 4.556 |
| WT HeLa infected with S. Typhi (3hs) | 26 | Titan Krios, 300keV, K3 camera, energy filter (20 eV), Volta phase plate (VPP) with −1 μm defocus | 3.384 |
| WT HeLa infected with S. Typhi-GtgE (1h) | 21 | Titan Krios, 300keV, K3 camera, energy filter (20 eV), Volta phase plate (VPP) with −1 μm defocus | 4.556 |
| WT BMDM infected with *S.* Typhi (1h) | 5 | Titan Krios, 300keV, K3 camera, energy filter (20 eV), Volta phase plate (VPP) with −1 μm defocus | 3.384 |
| WT BMDM infected with *S.* Typhi (1h) | 5 | Titan Krios, 300keV, K3 camera, energy filter (20 eV), Volta phase plate (VPP) with −1 μm defocus | 4.556 |
| WT BMDM infected with *S.* Typhi (3hs) | 15 | Titan Krios, 300keV, K3 camera, energy filter (20 eV), Volta phase plate (VPP) with −1 μm defocus | 4.556 |
| *Lrrk2*$^{-/-}$ BMDM infected with *S.* Typhi (3hs) | 18 | Titan Krios, 300keV, K3 camera, energy filter (20 eV), Volta phase plate (VPP) with −1 μm defocus | 4.556 |
| BLOC3$^{-/-}$ BMDM infected with *S.* Typhi (3hs) | 12 | Titan Krios, 300keV, K3 camera, energy filter (20 eV), Volta phase plate (VPP) with −1 μm defocus | 4.556 |

## Supplementary Material

Refer to Web version on PubMed Central for supplementary material.

## Acknowledgments

We thank Tukiet Lam and Weiwei Wang from the WM Keck Foundation Biotechnology Resource Laboratory at the Yale University School of Medicine, for assistance with the itaconate measurements. We also thank Meng Shao (Yale University) for assistance with the cryo-ET experiments. F.S was partially supported by a fellowship from the Human Frontiers Science Program (LT000056/2020-C). This work was supported by NIH Grants R01AI152421 and R01AI087946 to J. L., and R01AI114618 and R01AI055472 to J.E.G; and a pilot Grant from the Parkinson's Foundation (PF-RCE-1946). The Proteomics Resource of the WM Keck Foundation Biotechnology Resource Laboratory was partially supported by CTSA Grant Number UL1TR001863 from the National Center for Advancing Translational Sciences (NCATS) of the National Institutes of Health (NIH).

## Data availability:

Subtomogram-average density maps and the raw cryo-ET tilt series have been deposited in EMDB (deposition ID numbers: EMD-41046, EMD-41047, and EMPIAR-11577). The rest of the data are available in the main text, supplementary materials, and auxiliary files.

## References

1. Randow F, MacMicking J & James L Cellular self-defense: how cell-autonomous immunity protects against pathogens. Science 340, 701–706. (2013). [PubMed: 23661752]
2. Spanò S & Galán J A Rab32-dependent pathway contributes to Salmonella typhi host restriction. Science 338, 960–963 (2012). [PubMed: 23162001]
3. Tang B Rab32/38 and the xenophagic restriction of intracellular bacteria replication. Microbes Infect 18, 595–603 (2016). [PubMed: 27256464]
4. Li Y et al. Analysis of the Rab GTPase Interactome in Dendritic Cells Reveals Anti-microbial Functions of the Rab32 Complex in Bacterial Containment. Immunity 44, 422–437 (2016). [PubMed: 26885862]
5. Baldassarre M et al. The Rab32/BLOC-3-dependent pathway mediates host defense against different pathogens in human macrophages. Sci Adv 7, eabb1795 (2021). [PubMed: 33523895]
6. Chen M et al. Itaconate is an effector of a Rab GTPase cell-autonomous host defense pathway against Salmonella. Science 369, 450–455, doi:10.1126/science.aaz1333 (2020). [PubMed: 32703879]
7. Schuster EM et al. TFEB induces mitochondrial itaconate synthesis to suppress bacterial growth in macrophages. Nat Metab 4, 856–866, doi:10.1038/s42255-022-00605-w (2022). [PubMed: 35864246]
8. Michelucci A et al. Immune-responsive gene 1 protein links metabolism to immunity by catalyzing itaconic acid production. Proc Natl Acad Sci U S A 110, 7820–7825 (2013). [PubMed: 23610393]
9. Ruetz M et al. Itaconyl-CoA forms a stable biradical in methylmalonyl-CoA mutase and derails its activity and repair. Science 366, 589–593 (2019). [PubMed: 31672889]
10. Patel T & McFadden B Caenorhabditis elegans and Ascaris suum: Inhibition of isocitrate lyase by itaconate. Exp. Parasitol 44, 262–268 (1978). [PubMed: 658222]
11. McFadden B & Purohit S Itaconate, an isocitrate lyase-directed inhibitor in Pseudomonas indigofera. J Bacteriol 131, 136–144 (1977). [PubMed: 17593]
12. Cordes T et al. Immunoresponsive Gene 1 and Itaconate Inhibit Succinate Dehydrogenase to Modulate Intracellular Succinate Levels. J Biol Chem 291, 14274–14284 (2016). [PubMed: 27189937]
13. Wilson R & Maloy S Isolation and characterization of Salmonella typhimurium glyoxylate shunt mutants. J Bacteriol 169, 3029–3034 (1987). [PubMed: 3298210]

14. Fang F, Libby S, Castor M & Fung A Isocitrate lyase (AceA) is required for Salmonella persistence but not for acute lethal infection in mice. Infect Immun 73, 2547–2549 (2005). [PubMed: 15784602]
15. McKinney J et al. Persistence of Mycobacterium tuberculosis in macrophages and mice requires the glyoxylate shunt enzyme isocitrate lyase. Nature 406, 735–738 (2000). [PubMed: 10963599]
16. Mercado-Lubo R, Gauger E, Leatham M, Conway T & Cohen P A Salmonella enterica serovar typhimurium succinate dehydrogenase/fumarate reductase double mutant is avirulent and immunogenic in BALB/c mice. Infect. Immun 76, 1128–1134 (2008). [PubMed: 18086808]
17. Yimga M et al. Role of gluconeogenesis and the tricarboxylic acid cycle in the virulence of Salmonella enterica serovar typhimurium in BALB/c mice. Infect. Immun 74, 1130–1140 (2006). [PubMed: 16428761]
18. Pecsi I et al. Essentiality of succinate dehydrogenase in Mycobacterium smegmatis and its role in the generation of the membrane potential under hypoxia. MBio 5, pii: e01093–01014 (2014).
19. Hartman T et al. Succinate dehydrogenase is the regulator of respiration in Mycobacterium tuberculosis. PLoS Pathog 10, e1004510 (2014). [PubMed: 25412183]
20. Wheeler P Oxidation of carbon sources through the tricarboxylic acid cycle in Mycobacterium leprae grown in armadillo liver. J Gen Microbiol 130, 381–389 (1984). [PubMed: 6374022]
21. Reddick L & Alto N Bacteria fighting back: how pathogens target and subvert the host innate immune system. Mol Cell 54, 321–328 (2014). [PubMed: 24766896]
22. Finlay B & McFadden G Anti-immunology: evasion of the host immune system by bacterial and viral pathogens. Cell 124, 767–782 (2006). [PubMed: 16497587]
23. Spanò S, Gao X, Hannemann S, Lara-Tejero M & Galán J A Bacterial Pathogen Targets a Host Rab-Family GTPase Defense Pathway with a GAP. Cell Host Microbe 19, 216–226 (2016). [PubMed: 26867180]
24. Spano S, Liu X & Galan JE Proteolytic targeting of Rab29 by an effector protein distinguishes the intracellular compartments of human-adapted and broad-host Salmonella. Proc Natl Acad Sci U S A 108, 18418–18423, doi:10.1073/pnas.1111959108 (2011). [PubMed: 22042847]
25. Sasikaran J, Ziemski M, Zadora P, Fleig A & Berg I Bacterial itaconate degradation promotes pathogenicity. Nat. Chem. Biol 10, 371–377 (2014). [PubMed: 24657929]
26. Martin WR, Frigan F & Bergman EH Noninductive metabolism of itaconic acid by Pseudomonas and Salmonella species.. J. Bacteriol 82, 905–908 (1961). [PubMed: 14470458]
27. Parkhill J et al. Complete genome sequence of a multiple drug resistant Salmonella enterica serovar Typhi CT18. Nature 413, 848–852 (2001). [PubMed: 11677608]
28. Waschbüsch D et al. LRRK2 transport is regulated by its novel interacting partner Rab32. PLoS One 9, e111632 (2014). [PubMed: 25360523]
29. McGrath E, Waschbüsch D, Baker B & Khan A LRRK2 binds to the Rab32 subfamily in a GTP-dependent manner via its armadillo domain. Small GTPases 12, 133–146 (2021). [PubMed: 31552791]
30. Bui M et al. Rab32 modulates apoptosis onset and mitochondria-associated membrane (MAM) properties. J Biol Chem 285, 31590–31602 (2010). [PubMed: 20670942]
31. Zhang F et al. Identification of two new loci at IL23R and RAB32 that influence susceptibility to leprosy. Nat Genet 43, 1247–1251, doi:10.1038/ng.973 (2011). [PubMed: 22019778]
32. Singh A, Zhi L & Zhang H LRRK2 and mitochondria: Recent advances and current views. Brain Res 1702, 96–104 (2019). [PubMed: 29894679]
33. Gardet A et al. LRRK2 is involved in the IFN-gamma response and host response to pathogens. J. Immunol 185, 5577–5585 (2010). [PubMed: 20921534]
34. Shutinoski B et al. Lrrk2 alleles modulate inflammation during microbial infection of mice in a sex-dependent manner. Sci Transl Med 11, eaas9292 (2019). [PubMed: 31554740]
35. Liu W et al. LRRK2 promotes the activation of NLRC4 inflammasome during Salmonella Typhimurium infection. J Exp Med 214, 3051–3066 (2017). [PubMed: 28821568]
36. Weindel C et al. LRRK2 maintains mitochondrial homeostasis and regulates innate immune responses to Mycobacterium tuberculosis. Elife 9, e51071 (2020). [PubMed: 32057291]

37. Fava V et al. A missense LRRK2 variant is a risk factor for excessive inflammatory responses in Leprosy. PLOS Neglected Tropical Diseases 10, e0004412 (2016). [PubMed: 26844546]
38. Gao Y et al. The emerging role of Rab GTPases in the pathogenesis of Parkinson's disease. Mov Disord 33, 196–207 (2018). [PubMed: 29315801]
39. Manzanillo P et al. The ubiquitin ligase parkin mediates resistance to intracellular pathogens. Nature 7468, 512–516 (2013).
40. Ali S et al. PARK2/PACRG polymorphisms and susceptibility to typhoid and paratyphoid fever. Clin Exp Immunol 144, 425–431 (2006). [PubMed: 16734611]
41. Pickrell A & Youle R The roles of PINK1, parkin, and mitochondrial fidelity in Parkinson's disease. Neuron 2015 Jan 21;85(2):257–73. doi: 10.1016/j.neuron.2014.12.007. Neuron 85, 257–273 (2015). [PubMed: 25611507]
42. Nichols R LRRK2 Phosphorylation. Adv Neurobiol 14, 51–70 (2017). [PubMed: 28353278]
43. Galán JE & Curtiss III R Cloning and molecular characterization of genes whose products allow Salmonella typhimurium to penetrate tissue culture cells. Proc. Natl. Acad. Sc. USA 86, 6383–6387 (1989). [PubMed: 2548211]
44. Galan JE, Ginocchio C & Costeas P Molecular and functional characterization of the Salmonella invasion gene invA: homology of InvA to members of a new protein family. J Bacteriol 174, 4338–4349 (1992). [PubMed: 1624429]
45. Reith A et al. GSK2578215A; a potent and highly selective 2-arylmethyloxy-5-substitutent-N-arylbenzamide LRRK2 kinase inhibitor. Bioorg Med Chem Lett 22, 5625–5629 (2012 ). [PubMed: 22863203]
46. Leschziner A & Reck-Peterson S Structural Biology of LRRK2 and its Interaction with Microtubules. Mov Disord 36, 2494–2504 (2021). [PubMed: 34423856]
47. Harvey K & Outeiro T The role of LRRK2 in cell signalling. Biochem Soc Trans 47, 197–207 (2019). [PubMed: 30578345]
48. Degrandi D, Hoffmann R, Beuter-Gunia C & Pfeffer K The proinflammatory cytokine-induced IRG1 protein associates with mitochondria. J Interferon Cytokine Res 29, 55–67 (2009). [PubMed: 19014335]
49. Szeligowski R et al. Molecular evolution of IRG1 shapes itaconate production in metazoans and alleviates the "double-edged dilemma" of innate immune defense. bioRxiv 2022.06.17.496652 (2022).
50. Martin I et al. Ribosomal protein s15 phosphorylation mediates LRRK2 neurodegeneration in Parkinson's disease. Cell 157, 472–485, doi:10.1016/j.cell.2014.01.064 (2014). [PubMed: 24725412]
51. Lee J et al. Parkinson's disease-associated LRRK2-G2019S mutant acts through regulation of SERCA activity to control ER stress in astrocytes. Acta Neuropathol. Commun 7, 68 (2019). [PubMed: 31046837]
52. Gloeckner C & Porras P Guilt-by-Association - Functional Insights Gained From Studying the LRRK2 Interactome. Front Neurosci 14, 485 (2020). [PubMed: 32508578]
53. Mosaoa R, Kasprzyk-Pawelec A, Fernandez H & Avantaggiati M The Mitochondrial Citrate Carrier SLC25A1/CIC and the Fundamental Role of Citrate in Cancer, Inflammation and Beyond. Biomolecules 2021 Jan 22;11(2):141. doi: 10.3390/biom11020141. Biomolecules 11, doi:10.3390/biom11020141 (2021). [PubMed: 33499062]
54. Aluvila S, Sun J, Harrison DH, Walters DE & Kaplan RS Inhibitors of the mitochondrial citrate transport protein: validation of the role of substrate binding residues and discovery of the first purely competitive inhibitor. Mol Pharmacol 77, 26–34, doi:10.1124/mol.109.058750 (2010). [PubMed: 19843634]
55. Soubannier V et al. A vesicular transport pathway shuttles cargo from mitochondria to lysosomes. Curr. Biol 22, 135–141 (2012). [PubMed: 22226745]
56. Soto-Heredero G, Baixauli F & Mittelbrunn M Interorganelle Communication between Mitochondria and the Endolysosomal System. Front. Cell Dev. Biol 5, 95 (2017). [PubMed: 29164114]

57. Abuaita B, Schultz T & O'Riordan M Mitochondria-Derived Vesicles Deliver Antimicrobial Reactive Oxygen Species to Control Phagosome-Localized Staphylococcus aureus. Cell Host Microbe 24, 625–636 (2018). [PubMed: 30449314]
58. Klecker T, Böckler S & Westermann B Making connections: interorganelle contacts orchestrate mitochondrial behavior. Trends Cell Biol 24, 537–545 (2014 ). [PubMed: 24786308]
59. Wong Y, Kim S, Peng W & Krainc D Regulation and Function of Mitochondria-Lysosome Membrane Contact Sites in Cellular Homeostasis. Trends Cell Biol 29, 500–513 (2019). [PubMed: 30898429]
60. Wozny MR et al. Supramolecular architecture of the ER-mitochondria encounter structure in its native environment. bioRxiv, 2022.2004.2012.488000, doi:10.1101/2022.04.12.488000 (2022).
61. Collado J & Fernandez-Busnadiego R Deciphering the molecular architecture of membrane contact sites by cryo-electron tomography. Biochim Biophys Acta Mol Cell Res 1864, 1507–1512, doi:10.1016/j.bbamcr.2017.03.009 (2017). [PubMed: 28330771]
62. Daniele T et al. Mitochondria and melanosomes establish physical contacts modulated by Mfn2 and involved in organelle biogenesis. Curr Biol 24, 393–403 (2014). [PubMed: 24485836]
63. Li M, Tripathi-Giesgen I, Schulman B, Baumeister W & Wilfling F In situ snapshots along a mammalian selective autophagy pathway. Proc Natl Acad Sci U S A 120, e2221712120 (2023). [PubMed: 36917659]
64. Dhekne H et al. LRRK2-phosphorylated Rab10 sequesters Myosin Va with RILPL2 during ciliogenesis blockade. Life Sci Alliance, e202101050 (2021).
65. Esteves A & Cardoso S LRRK2 at the Crossroad Between Autophagy and Microtubule Trafficking: Insights into Parkinson's Disease. Neuroscientist 23, 16–26 (2017). [PubMed: 26740081]
66. Caesar M et al. Leucine-rich repeat kinase 2 functionally interacts with microtubules and kinase-dependently modulates cell migration. Neurobiol Dis 54, 280–288 (2013). [PubMed: 23318930]
67. Toyofuku T, Okamoto Y, Ishikawa T, Sasawatari S & Kumanogoh A LRRK2 regulates endoplasmic reticulum-mitochondrial tethering through the PERK-mediated ubiquitination pathway. EMBO J 39, e100875 (2020). [PubMed: 31821596]
68. Rocha EM, Keeney MT, Di Maio R, De Miranda BR & JT., G. LRRK2 and idiopathic Parkinson's disease. Trends Neurosci 45, 224–236 (2022). [PubMed: 34991886]
69. Benson DL, Matikainen-Ankney BA, Hussein A & GW., H. Functional and behavioral consequences of Parkinson's disease-associated LRRK2-G2019S mutation. Biochem Soc Trans 46, 1697–1705 (2018). [PubMed: 30514770]
70. Galan JE & Curtiss R 3rd. Distribution of the invA, -B, -C, and -D genes of Salmonella typhimurium among other Salmonella serovars: invA mutants of Salmonella typhi are deficient for entry into mammalian cells. Infect Immun 59, 2901–2908 (1991). [PubMed: 1879916]
71. Hoiseth SK & Stocker BA Aromatic-dependent Salmonella typhimurium are non-virulent and effective as live vaccines. Nature 291, 238–239 (1981). [PubMed: 7015147]
72. Kaniga K, Bossio JC & Galan JE The Salmonella typhimurium invasion genes invF and invG encode homologues of the AraC and PulD family of proteins. Mol Microbiol 13, 555–568 (1994). [PubMed: 7997169]
73. Demarre G et al. A new family of mobilizable suicide plasmids based on broad host range R388 plasmid (IncW) and RP4 plasmid (IncPα) conjugative machineries and their cognate Escherichia coli host strains. Res. Microbiol 156, 245–255 (2005). [PubMed: 15748991]
74. Galán JE & Curtiss III R Expression of Salmonella typhimurium genes required for invasion is regulated by changes in DNA supercoiling. Infect. Immun 58, 1879–1885 (1990). [PubMed: 2160435]
75. Gibson D et al. Enzymatic assembly of DNA molecules up to several hundred kilobases. Nat Methods 6, 343–345 (2009). [PubMed: 19363495]
76. Chang S, Song J & Galán J Receptor-Mediated Sorting of Typhoid Toxin during Its Export from Salmonella Typhi-Infected Cells. Cell Host Microbe 20, 682–689 (2016). [PubMed: 27832592]
77. Ran FA et al. Genome engineering using the CRISPR-Cas9 system. Nat Protoc 8, 2281–2308, doi:10.1038/nprot.2013.143 (2013). [PubMed: 24157548]

78. Obert S, O'Connor RJ, Schmid S & Hearing P The adenovirus E4–6/7 protein transactivates the E2 promoter by inducing dimerization of a heteromeric E2F complex. Molec. Cell. Biol 14, 1333–1346 (1994). [PubMed: 8289811]
79. Schnitzbauer J, Strauss M, Schlichthaerle T, Schueder F & Jungmann R Super-resolution microscopy with DNA-PAINT. Nat Protoc 12, 1198–1228 (2017). [PubMed: 28518172]
80. Lampropoulou V et al. Itaconate Links Inhibition of Succinate Dehydrogenase with Macrophage Metabolic Remodeling and Regulation of Inflammation. Cell Metab 24, 158–166 (2016 ). [PubMed: 27374498]
81. Mastronarde D Automated electron microscope tomography using robust prediction of specimen movements.. J Struct Biol 152, 36–51 (2005). [PubMed: 16182563]
82. Zheng S et al. MotionCor2: anisotropic correction of beam-induced motion for improved cryo-electron microscopy. Nat Methods 14, 331–332 (2017). [PubMed: 28250466]
83. Morado D, Hu B & Liu J Using Tomoauto: A Protocol for High-throughput Automated Cryo-electron Tomography. J Vis Exp 107, e53608, doi:10.3791/53608. (2016).
84. Kremer J, Mastronarde D & McIntosh J Computer visualization of three-dimensional image data using IMOD. J. Struct. Biol 116, 71–76 (1996). [PubMed: 8742726]
85. Winkler H 3D reconstruction and processing of volumetric data in cryo-electron tomography. J Struct Biol 157, 126–137 (2007). [PubMed: 16973379]
86. Goddard TD et al. UCSF ChimeraX: Meeting modern challenges in visualization and analysis. Protein Sci 27, 14–25, doi:10.1002/pro.3235 (2018). [PubMed: 28710774]
87. Chen M et al. Convolutional neural networks for automated annotation of cellular cryo-electron tomograms. Nat Methods 14, 983–985, doi:10.1038/nmeth.4405 (2017). [PubMed: 28846087]
88. Chen M et al. Convolutional neural networks for automated annotation of cellular cryo-electron tomograms. Nat Methods 14, 983–985 (2017). [PubMed: 28846087]
89. Goddard T et al. UCSF ChimeraX: Meeting modern challenges in visualization and analysis. Protein Sci 27, 14–25 (2018 ). [PubMed: 28710774]
90. Liu Y-T et al. Isotropic reconstruction for electron tomography with deep learning. Nature Communications 13, 6482, doi:10.1038/s41467-022-33957-8 (2022).

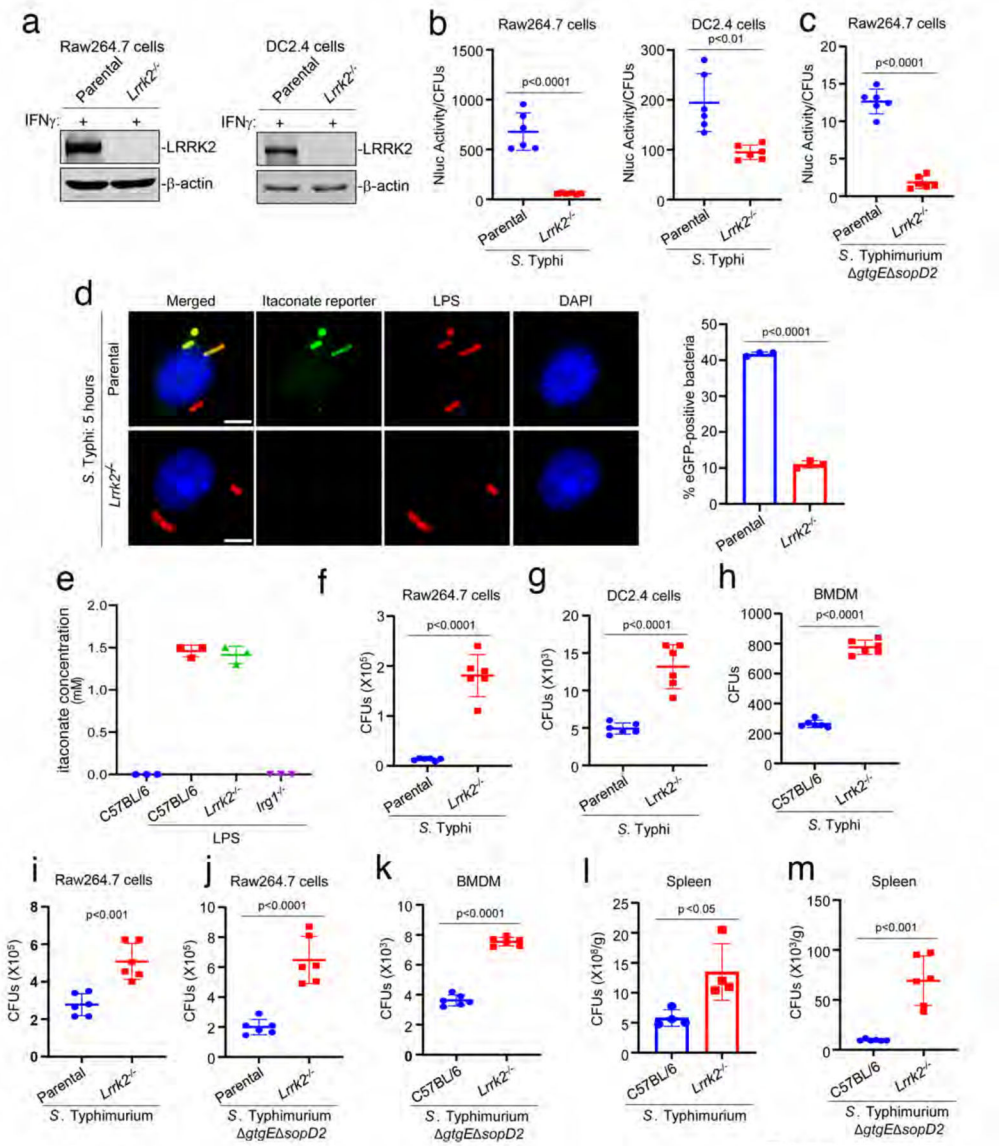


**Fig. 1: LRRK2 is a component of the RAB32-dependent host defense pathway against *Salmonella*.**

(**a**) Western blot analysis of cell lysates of parental and CRISPR/Cas9-generated *Lrrk2*$^{-/-}$ Raw264.7 or DC2.4 cells. (**b** and **c**) Raw264.7 or DC2.4 parental (control) and *Lrrk2*$^{-/-}$ cells were infected with either wild-type *S.* Typhi (**b**) (MOI = 6) or *S.* Typhimurium Δ*gtgE* Δ*sopD2* mutant strain (MOI = 3) (**c**) encoding a luciferase-based itaconate biosensor, and the levels of luciferase in the cell lysates were measured 20 hs after infection. Each circle or square represents a single luciferase measurement. The mean ± SD and *p* values of the indicated comparisons (unpaired two-tailed Student's t test) are shown. (**d**) Alternatively, Raw264.7 parental (control) and *Lrrk2*$^{-/-}$ cells were infected with *S.* Typhi strains encoding an eGFP-based itaconate biosensor (MOI = 6) and the percentage of bacterial cells expressing eGFP were determined 5 hs after infection. Each square and circle represent the mean of an individual experiment in which at least 200 infected cells were examined. The *p* value (unpaired two-tailed Student's t test) of the indicated comparison is shown.

Infected cells were fixed, stained with DAPI (blue) to visualize nuclei, and stained with an anti-*Salmonella* LPS antibody along with Alexa 594-conjugated anti-rabbit antibody (red) to visualize all bacteria. Representative fields of infected cells are shown (scale bar = 5 μm). (**e**) Itaconate levels in BMDMs obtained from the indicated mice before and after LPS treatment to induce the expression of IRG1. Values represent the mean ± SD of three independent measurements. (**f-k**) Raw264.7 or DC2.4 parental (control) and *Lrrk2*$^{-/-}$ cells, as well as bone marrow-derived macrophages (BMDM) from C57BL/6 or *Lrrk2*$^{-/-}$ mice were infected with either wild-type *S.* Typhi (MOI = 6, wild type *S.* Typhimurium (MOI = 3), or an *S.* Typhimurium Δ*gtgE* Δ*sopD2* mutant strain (MOI = 3) (as indicated) and the number of CFU was determined 20 hs after infection. Each square or circle represents the CFU in an independent measurement. The mean ± SD and *p* values (unpaired two-tailed Student's t test) of the indicated comparisons are shown. (**l** and **m**) C57BL/6 or *Lrrk2*$^{-/-}$ mice were intraperitoneally infected with wild-type *S.* Typhimurium or the Δ*gtgE* Δ*sopD2* isogenic mutant derivative ($10^2$ CFU), and 4 days after infection bacterial loads in the spleen of the infected animals were determined. Each circle or square represents the CFU of the spleen of an individual animal. The mean ± SD and *p* values (unpaired two-tailed Student's t test) of the indicated comparisons are shown.

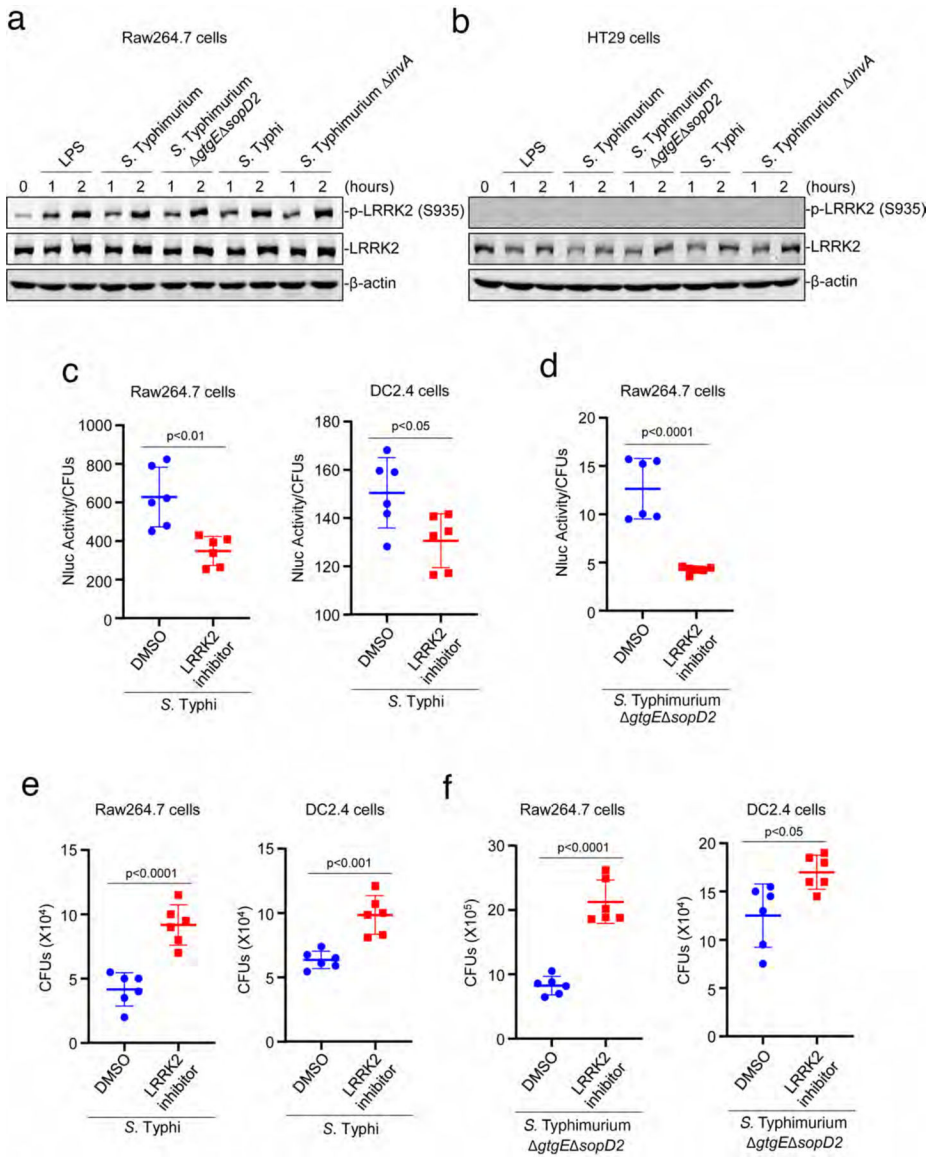


**Fig. 2: The kinase activity of LRRK2 is required for its contribution to the RAB32-dependent pathogen restriction pathway.**

(**a** and **b**) Raw264.7 or HT29 cells were treated with LPS or infected with the indicated bacterial strains for the indicated times. The activation of LRRK2, assessed by its phosphorylation at S935, was then analyzed by immunoblotting with the indicated antibodies. (**c** and **d**) Raw264.7 or DC2.4 cells were pre-treated with the LRRK2 inhibitor GSK2578215A for 90 min, infected with either wild-type *S.* Typhi (MOI = 6) (**c**) or the *S.* Typhimurium Δ*gtgE* Δ*sopD2* mutant strain (MOI = 3) (**d**), both encoding a luciferase-based itaconate biosensor, and the levels of luciferase in the cell lysates were measured 20 hs after infection. Each circle or square represents a single luciferase measurement. The mean ± SD and *p* values (unpaired two-tailed Student's t test) of the indicated comparisons are shown. (**e** and **f**) Raw264.7 or DC2.4 cells were pre-treated with the LRRK2 inhibitor GSK2578215A for 90 min, infected with wild-type *S.* Typhi (MOI = 6) (**e**) or the *S.* Typhimurium Δ*gtgE* Δ*sopD2* mutant strain (MOI = 3) (**f**), and the number of CFU was

determined 20 hs after infection. Each circle or square represents a single measurement. The mean ± SD and the *p* values (unpaired two-tailed Student's *t* test) of the indicated comparisons are shown.

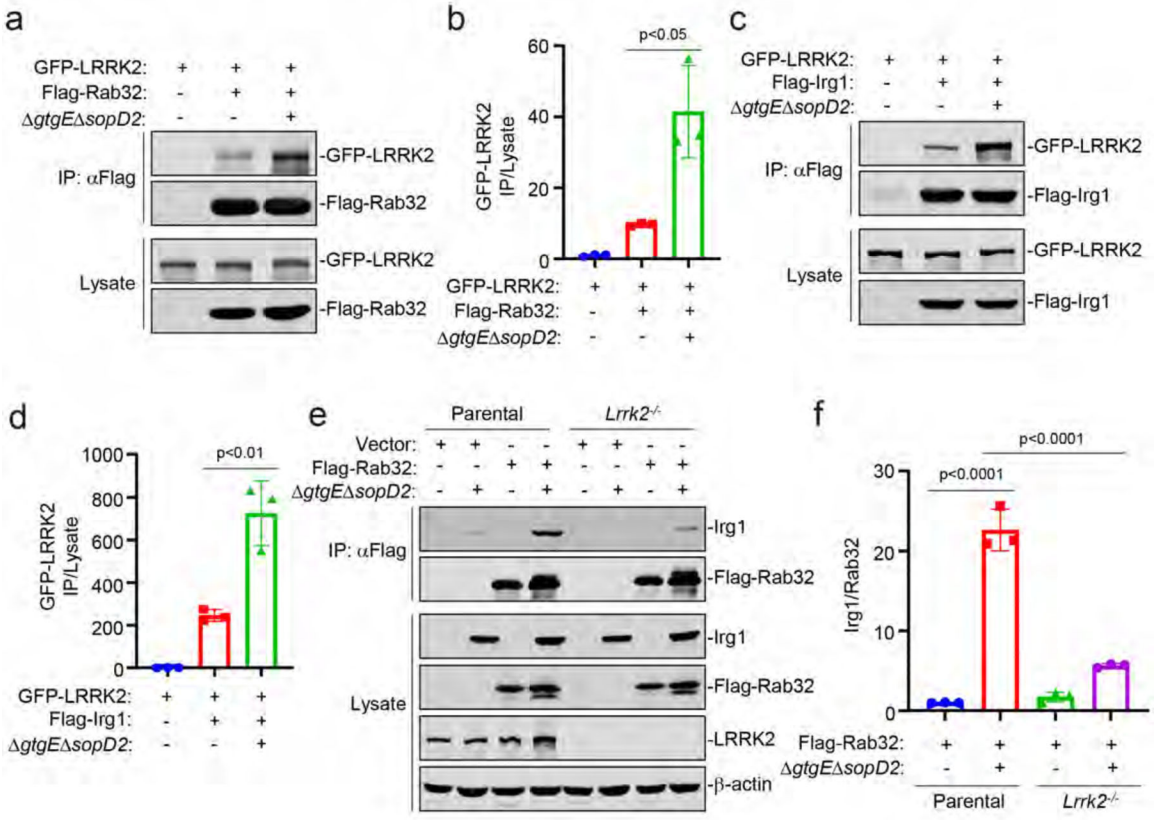


**Fig. 3: LRRK2 scaffolds the formation of RAB32-IRG1 complex.**

(**a** and **b**) LRRK2 interacts with RAB32. HEK293T cells were transiently co-transfected with a plasmid expressing GFP-LRRK2 and a plasmid expressing FLAG-RAB32. Twenty hours after transfection cells were infected with the *S.* Typhimurium Δ*gtgE* Δ*sopD2* mutant strain (MOI = 3) and 4 hs after infection, cell lysates were analyzed by immunoprecipitation and immunoblotting with antibodies against the FLAG epitope and GFP, respectively. The quantification of the intensity of the GFP-LRRK2 band is shown in (**b**). Each circle, square, or triangle represents a measurement in an independent experiment. The mean ± SD and *p* values (unpaired two-tailed Student's *t* test) of the indicated comparisons are shown. (**c** and **d**) LRRK2 interacts with IRG1. HEK293T cells were transiently co-transfected with a plasmid expressing GFP-LRRK2 and a plasmid expressing FLAG-IRG1. Twenty hours after transfection cells were infected with the *S.* Typhimurium Δ*gtgE* Δ*sopD2* mutant strain (MOI = 3) and 4 hs after infection, cell lysates were then analyzed by immunoprecipitation and immunoblotting with antibodies against the FLAG epitope and GFP, respectively. The quantification of the intensity of the GFP-LRRK2 band is shown in (**d**). Each circle, square, or triangle represents a measurement in an independent experiment. The mean ± SD and *p* values (unpaired two-tailed Student's *t* test) of the indicated comparisons are shown. (**e** and **f**) LRRK2 promotes the formation of the RAB32-IRG1 complex. Raw264.7 parental (control) or *Lrrk2*$^{-/-}$ cells stably expressing FLAG-RAB32 were left uninfected or infected with the *S.* Typhimurium Δ*gtgE* Δ*sopD2* mutant strain (MOI = 3) for 18 hs. Cell lysates were then analyzed by immunoprecipitation and immunoblotting with antibodies against the FLAG epitope, endogenous IRG1 or LRRK2, and β-actin (as a loading control). The

quantification of the intensity of the Irg1 band relative to the intensity of the RAB32 band is shown in (**f**). Each circle, square, or triangle represents a measurement in an independent experiment. The mean ± SD and *p* values (unpaired two-tailed Student's *t* test) of the indicated comparisons are shown.

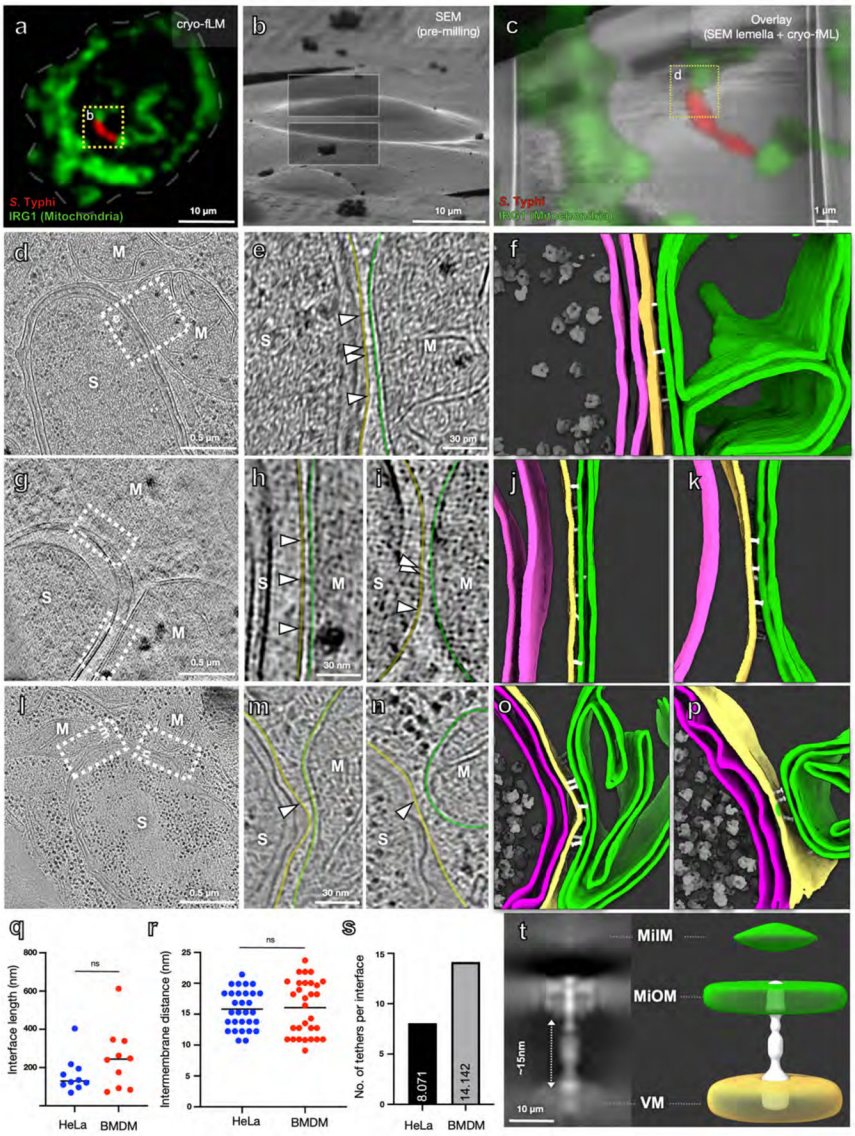


**Fig. 4: Intimate association of the SCV with the mitochondria observed by cryo-electron tomography.**

(**a**) Cryo-fluorescence microscopy (cryo-fLM) of cultured HeLa cells stably expressing IRG1-GFP (green) and infected with *S.* Typhi encoding an mCherry itaconate biosensor (red). Specimen were vitrified in liquid ethane 3 hs post infection. White dashed line marks the cell boundary. The yellow-dotted square region was targeted for further imaging analysis. (**b**) Scanning electron microscopy (SEM) image of the *S.* Typhi infected HeLa cell shown in Panel (**a**) before cryo-focused ion beam (cryo-FIB) milling. Two rectangular boxes show areas targeted for ablation during the cryo-FIB milling. (**c**) SEM image of the cryo-lamella (<200nm thick) containing the target bacteria. Cryo-fLM signals (green: IRG1-GFP; red: mCherry itaconate biosensor) are overlayed on the SEM image. (**d**) Cryo-electron tomography (cryo-ET) image of the highlighted area in panel (**c**) showing close association of the SCV and mitochondria. (**e-f**) Intermembrane tethers bridge the SCV-mitochondria interface. (**e**) Zoom-in image of the tomographic slice at

the SCV-mitochondria interface highlighted in Panel (**d**). Yellow and green transparent lines overlay the vacuolar and mitochondria membranes, respectively. White arrows denote the intermembrane tethers. (**f**) 3-dimentional rendering of the SCV-mitochondria interface (z=110 slices). Bacterial, vacuolar, and mitochondrial membranes are shown in magenta, yellow, and green, respectively, bacterial ribosomes are shown in grey and intermembrane tethers are shown in white. Following the subtomogram averaging of the intermembrane tethers, segmented volume of the tether was mapped back into the original tomogram using the recalculated coordinates and Euler parameters. (**g-k**) Additional examples of SCV-mitochondria association in HeLa cells. Cryo-ET image showing close association of the SCV and mitochondria (**g**). The indicated zoom-in regions of the tomographic slice at the SCV-mitochondria interfaces are shown in (**h-i**), and the corresponding 3-dimentional renderings are shown in (**j-k**) (z=197 slices). The color scheme indicating bacterial, vacuolar, and mitochondrial membranes, bacterial ribosomes and intermembrane tethers is as indicated in (**f**). (**l-p**) Intermembrane tethers are also observed at the SCV-mitochondrial interface in BMDM infected with *S.* Typhi. BMDM isolated from C57BL/6 mice were cultured on cryo-EM grids and infected with *S.* Typhi encoding the mCherry itaconate biosensor for 1 h, and mCherry expressing *S.* Typhi cells were targeted for cryo-FIB milling and cryo-ET imaging. (**l**) Cryo-ET image showing close association of the SCV and mitochondria. The indicated zoom-in regions of the tomographic slice at the SCV-mitochondria interfaces are shown in (**m**) and (**n**), and the corresponding 3-dimentional renderings are shown in (**o**) and (**p**) (z=88 slices). (**q**) Measurement of the length of the vacuolar membrane (VM) and mitochondrial outer membrane (MiOM) interface. The X-Y plane density profiling function in tomographic software IMOD was used to measure the maximum length of the intimate contact between the VM and MiOM in both HeLa (blue) and BMDM (red) cells. Measurements were taken in 10 interfaces (N=10) from 3 independent experiments for both HeLa and BMDM cells. Dots in this scatter dot plot represent raw data. Solid lines within the box represent mean values (HeLa: 163.5 ± 95.6 nm, BMDM: 247.2 ± 162.7 nm). Welch's t-test resulted in $p$-value of 0.1291 which suggest no significant difference between the distance that VM and MiOM makes contact in HeLa and BMDMs. (**r**) Measurement of the intermembrane distance between vacuolar membrane (VM) and the mitochondrial outer membrane (MiOM). The X-Y plane density profiling function in tomographic software IMOD was used to measure distance between VM and MiOM in both HeLa (blue) and BMDM (red). Measurements were taken at 30 interfaces (N=30) from three independent experiments in both HeLa and BMDM cells. Dots in this scatter dot plot represent raw data. Solid lines within the box represent mean values (HeLa: 15.82 ± 3.04nm, BMDM: 16.06 ± 4.35). Welch's t-test resulted in p-value of 0.8098 which suggest no significant difference between the intermembrane spacings measured in HeLa and BMDMs. (**s**) Quantification of intermembrane tethers in HeLa and BMDMs. Positions of intermembrane tethers are identified as a part of particle picking procedure for the subsequent subtomogram averaging. Number of intermembrane tethers in both HeLa and BMDMs are divided by the total number of mitochondria that show visible intermembrane tethers. (**t**) 2- and 3-dimentional cross section of the subtomogram average map. The vertical length of the tether perpendicular to the membranes is ~15nm. Mitochondrial inner (MiIM) and outer (MiOM) membranes are shown in green and the SCV membrane (VM) is shown in yellow. M: mitochondria; S: *S.* Typhi.

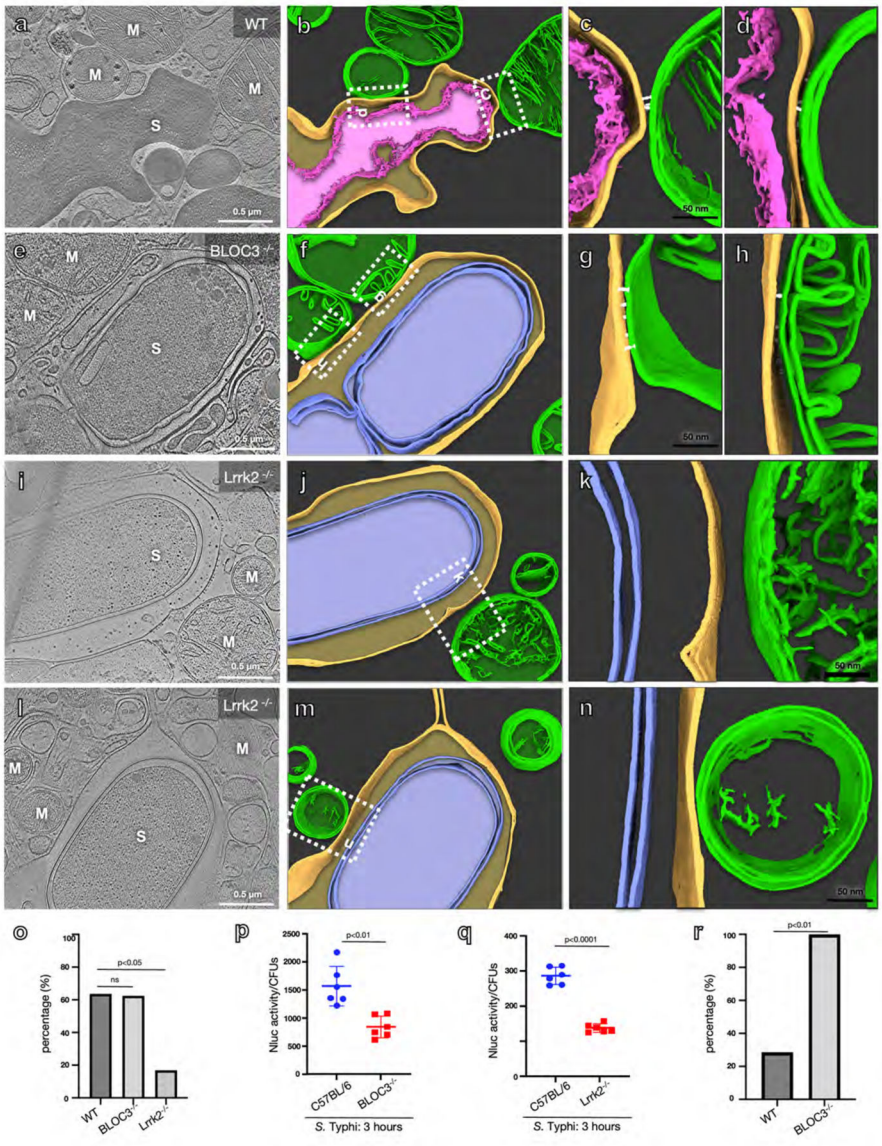


**Fig. 5: LRRK2 is required for establishing a close association between the SCV and the mitochondria.**

(**a-n**) Cryo-ET images showing the SCV and mitochondria in BMDMs obtained from C57BL/6 (**a-d**), BLOC3$^{-/-}$ (**e-h**), and *Lrrk2*$^{-/-}$ (**l-n**) mice, infected for 3 hs with a wild-type *S.* Typhi strain constitutively expressing mScarlet. Tomograms are shown in (**a**, **e, i, l**), and their respective 3D-renderings in (**b-d**, z=61slices, **f-h**, z=51 slices, **j-k**, z=50 slices, and **m-n**, z=71 slices) for C57BL/6 (WT), BLOC3$^{-/-}$, and *Lrrk2*$^{-/-}$ BMDMs, as indicated. The SCV membrane is shown in yellow, mitochondria are shown in green, and inter-membrane tethers in white. Note the altered *S.* Typhi bacterial cell envelope architecture (denoted in pink) in BMDMs from C57BL/6 mice, and its normal appearance (denoted in blue) in BLOC3$^{-/-}$, or *Lrrk2*$^{-/-}$ BMDMs. Also, while intermembrane tethers are readily visualized linking the mitochondria and the SCV in BMDMs from C57BL/6 and BLOC3$^{-/-}$ mice (highlighted in zoomed in panels **c**, **d**, **g**, and **h**), no tethers were visualized in BMDMs from *Lrrk2*$^{-/-}$ mice (**i-n**), even in the rare occasions when mitochondria and SCVs were

seen in close proximity (**l-n**). (**o**) Quantification of the percentage of SCVs making intimate contact (a distance of ≤ 25nm) with mitochondria as observed by cryo-ET. A total of 32 cells were analyzed from two independent experiments in WT, BLOC3$^{-/-}$, and *Lrrk2*$^{-/-}$ BMDM cells. Unpaired *t*-test was used to determine the statistical significance. n. s.: difference not statistically significant ($p$=0.8721). (**p** and **q**) Itaconate delivery to the SCV in BMDMs obtained from C57BL/6, BLOC3$^{-/-}$, or *Lrrk2*$^{-/-}$ mice (as indicated). BMDMs were infected with wild type *S.* Typhi (MOI = 6) encoding a luciferase-based itaconate biosensor and the levels of luciferase in the cell lysates were measured 3 hs after infection. Each circle or square represents a single luciferase measurement. The mean ± SD and $p$ values of the indicated comparisons (unpaired two-tailed Student's t test) are shown. (**r**) Quantification of the percentage of bacteria contained within SCVs in close contact with mitochondria that show envelope alterations. A total of 21 bacteria were examined in two independent experiments with WT and BLOC3$^{-/-}$ BMDMs cells. Unpaired *t*-test was used to determine the statistical significance ($p$=0.0045).

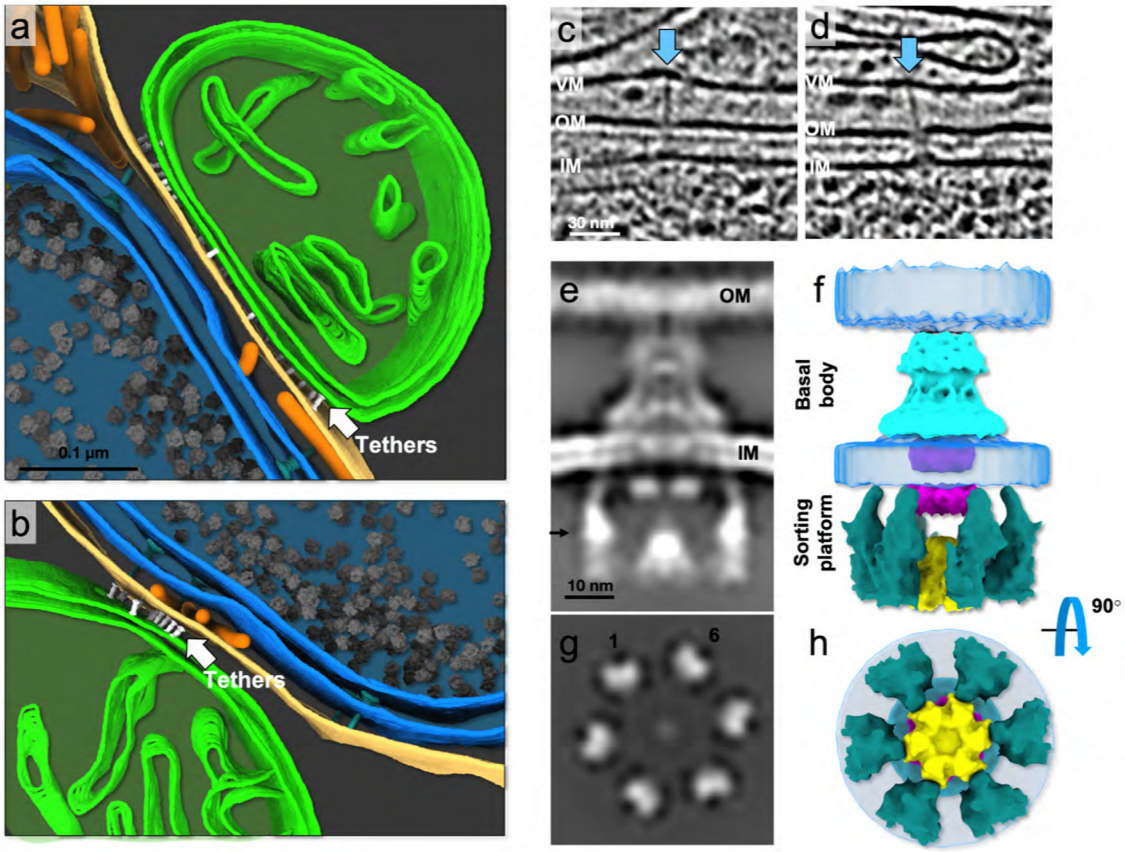


**Fig. 6. *Salmonella* deploys its type III secretion system at the SCV-mitochondria interface.**

(**a** and **b**) 3D-rendering of a close up of the mitochondria-SCV interface. Depicted are the intermembrane tethers (in white and denoted by white arrows) and the bacterial type III secretion machines encoded in its pathogenicity island 1 (in blue) (z=86 slices). (**c** and **d**) Tomographic slices showing the T3SS injectisomes deployed at the SCV-mitochondria interface. The sites where the needle tips make contact with the SCV membrane are marked with blue arrows. (**e-h**) Subtomogram average structure of the injectisome showing an assembled sorting platform, an indication of an active type III secretion machine. 2D vertical cross-section (**e**) and 3D rendering (**f**) of the subtomogram average show the needle complex base and the cytoplasmic sorting platform. 2D horizontal cross-section of the sorting platform at the position indicated with an arrow in panel (**e**) is shown in **(g)** and its 3D-rendering is shown (**h**) depicting the 6-fold symmetric pods (green) and central ATPase (yellow). The export apparatus component InvA is depicted in cyan, and bacterial membranes are colored in transparent blue.